

1 Local wind regime induced by giant linear dunes:
2 comparison of ERA5 re-analysis with surface
3 measurements

4 Cyril Gadal · Pauline Delorme ·
5 Clément Narteau · Giles F.S. Wiggs ·
6 Matthew Baddock · Joanna M. Nield ·
7 Philippe Claudin

8
9 Received: DD Month YEAR / Accepted: DD Month YEAR

10 **Abstract**

11 Emergence and growth of sand dunes ~~result from the interaction between the~~
12 ~~topography, which perturbs the wind flow, which itself controls the results~~
13 ~~from the dynamic interaction between topography, wind flow and~~ sediment
14 transport. While ~~these feedbacks~~ feedbacks between these variables are well
15 studied at the scale of a single dune, the average effect of a periodic dune
16 pattern on atmospheric flows remains poorly constrained due to a lack of data
17 in major sand seas. Here, we compare field measurements of surface wind data
18 to the predictions of the ERA5-Land climate reanalysis ~~in four different places~~
19 at four locations in Namibia, ~~inside and north of~~ including within the giant-
20 dune field of the Namib sand sea. In the ~~flat desert areas~~ desert plains to

C. Gadal

Institut de Mécanique des Fluides de Toulouse, Université de Toulouse Paul Sabatier, CNRS,
Toulouse INP-ENSEEIHT, Toulouse, France. E-mail: cyril.gadal@imft.fr

P. Delorme

School of Geography and Environmental Science, University of Southampton, Southampton,
UK.

C. Narteau

Institut de Physique du Globe de Paris, Université de Paris, CNRS, Paris, France.

G. S.F.-Wiggs

School of Geography and the Environment, University of Oxford, Oxford, UK.

M. Baddock

Geography and Environment, Loughborough University ~~of Technology~~, Loughborough, UK.

J.M. Nield

School of Geography and Environmental Science, University of Southampton, Southampton,
UK.

P. Claudin

Physique et Mécanique des Milieux Hétérogènes, CNRS, ESPCI Paris, PSL Research
University, Université de Paris, Sorbonne Université, Paris, France. E-mail:
philippe.claudin@espci.fr

21 the north of the sand sea, observations and predictions agree well ~~despite the~~
22 ~~small amount of data in the assimilation process~~. This is also the case in the
23 interdune areas of the sand sea, except for the weak winds blowing at night in a
24 direction oblique to the orientation of the giant dunes, which exhibit additional
25 components aligned with the giant dune orientation, which are not predicted
26 by the ERA5-Land reanalysis. We quantify these similarities and differences
27 and provide a physical understanding of the relevant aerodynamical regimes to
28 relate them to the daily cycle of the turbulent atmospheric boundary layer over
29 a dune pattern of given wavelength. We conclude by identifying the conditions
30 under which the ERA5-Land reanalysis data can ~~or can't reliably~~ be used
31 to study dune morphodynamics. We also propose that, in multidirectional
32 wind regimes, deflections of specific winds by giant dunes could explain the
33 occurrence of secondary dune patterns with a different orientation than to the
34 primary structures between which they grow develop.

35 **Keywords** Atmospheric boundary layer · Sand dunes · Fluid-structure
36 interactions

37 1 Introduction

38 The description of turbulent flows over a complex topography is a rich and
39 active subject, that is relevant for a large variety of different environmental
40 systems (Finnigan et al. 2020). For example, the flow over hills is of primary
41 interest for wind power, meteorological and air pollution phenomena (Taylor
42 et al. 1987). The properties of these flows are also key to the understanding of
43 the formation of ocean surface wind-driven waves (Sullivan and McWilliams
44 2010), dissolution bedforms (Claudin et al. 2017), or sedimentary ripples and
45 dunes (Charru et al. 2013; Courrech du Pont 2015). Importantly, the tropo-
46 sphere presents a vertical structure, with a lower convective boundary layer,
47 of typical kilometer-scale thickness, capped by a stably stratified region (Stull
48 1988). The largest topographic obstacles, such as mountains can therefore in-
49 teract with this upper region, for example leading and lead to internal wave
50 generation or significant wind disturbances, such as downslope winds in lee
51 sides lee-side downslope winds (Durran 1990).

52 Looking at Focusing on the wind close to the surface, two related topo-
53 graphic feedbacks on the flow, although related, windflow over dunes can
54 be commented separately. There is a first effect on the wind intensity: the
55 flow accelerates on the upwind slope and slows down on the downwind one
56 (?)on separately. First is the effect on wind speed with documented flow
57 acceleration on upwind slopes (Weaver and Wiggs 2011) and deceleration on
58 downwind slopes (Baddock et al. 2007), with a speed-up factor essentially pro-
59 portional to the obstacle aspect ratio here a ref? (Jackson and Hunt 1975).
60 Importantly, the velocity maximum is typically shifted upwind of the ob-
61 stacle crest. This behaviour has been theoretically predicted by means of
62 asymptotic analysis of a neutrally stratified boundary-layer flow over an ob-
63 stacle of vanishing aspect ratio (Jackson and Hunt 1975; Mason and Sykes
64 1979; Sykes 1980; Hunt et al. 1988; Belcher and J.C.R. 1998). Experiments
65 in flumes (Zilker et al. 1977; Zilker and Hanratty 1979; Frederick and Han-
66 ratty 1988; Poggi et al. 2007), in wind tunnel tunnels (Gong and Ibbet-
67 son 1989; Finnigan et al. 1990; Gong et al. 1996) and in field conditions
68 (Taylor and Teunissen 1987; Clauudin et al. 2013; Fernando et al. 2019; Lü et al. 2021) (Taylor and Teunissen 1987; Clauudin et al. 2013; Fernando et al. 2019; Lü et al. 2021)
69 have also documented this effect. Interestingly, a similar behaviour exists for
70 the pressure perturbation, but with a slight downwind shift for the pressure
71 minimum (Claudin et al. 2021). The second effect, much less studied, is the
72 flow deflection that occurs when the incident wind direction is not perpen-
73 dicular to the ridge crest. While predicted to be small (less than 10°) in the
74 linear regime valid for shallow topography (Gadal et al. 2019), significant flow
75 steering has been reported in the field on the downwind side of steep enough
76 obstacles, such as mountain ranges (Kim et al. 2000; Lewis et al. 2008; Fer-
77 nando et al. 2019) or well developed well-developed sand dunes (Walker et al.
78 2009; Hesp et al. 2015; Walker et al. 2017; Smith et al. 2017), and valley
79 topographies (Wiggs et al. 2002).

80 For practical reasons, wind measurement over sand dunes have has been
81 performed over rather small bedforms, typically a few meters high only – that

is (corresponding to tens of meters in length long) (Wiggs et al. 1996). Giant dunes, with kilometer-scale wavelengths and heights of tens of meters, are more difficult to investigate although they provide, for several reasons, they provide a choice configuration for the study of turbulent flows over a complex topography. First of all, one expects larger wind disturbances for larger obstacles. Second, their large size makes them interact with the vertical structure of the atmosphere (?). Also (Andreotti et al. 2009). Third, they usually form large patterns in sand seas and thus behave as rather clean periodic perturbations, in contrast with isolated hills dunes. Finally, because the morphodynamics of aeolian bedforms are strongly dependent on the local wind regime (?) (Livingstone and Warren 2019), one can expect to see the consequences of the wind disturbances on smaller windflow disturbance by large dunes on neighbouring small dunes, in a similar way as what has been manner to that reported for the effect of dunes on impact ripples (Howard 1977; Hood et al. 2021).

Arid areas Atmospheric flows have been much studied at the desert scale from desert-scale with climate reanalyses based on global atmospheric models (Blumberg and Greeley 1996; Livingstone et al. 2010; Ashkenazy et al. 2012; Jolivet et al. 2021; Hu et al. 2021), such as ERA-40, ERA-Interim or ERA-5 (Uppala et al. 2005; Dee et al. 2011; Hersbach et al. 2020). However, the spatial resolution (tens of kilometers) of these reanalyses implies average quantities that do not resolve the smaller scales, ranging from individual dunes to the border of mountains (Livingstone et al. 2010). Lately Recently, the release of ERA5-Land allows to push back has resolved this limitation by providing up to 70 years of hourly wind predictions at a 9 km spatial resolution (Muñoz-Sabater et al. 2021). However, its validity remains to be studied, especially in remote desert areas where data assimilation is low (such as deserts) very low.

In this work, we compare local wind speeds and directions measured in four different places by meteorological stations at four different locations inside and north of the giant-dune field of the Namib sand sea to the regional predictions of the ERA5-Land climate reanalysis. When Where the meteorological stations are surrounded by a relatively flat environment, we show that local measurements and regional predictions agree well with each other. The find that the agreement is also good in the interdune areas of the sand sea, except for the some weak winds blowing at night in a direction oblique to the orientation of the giant dunes, which exhibit an additional component aligned with the giant dune orientation, which are not predicted by the ERA5Land reanalysis (section 2). Furthermore Further, we are able to link the magnitude of these differences to the circadian cycle of the atmospheric boundary layer (section 3). Finally, we draw implications of for the wind disturbances on smaller-scale dunes (section 4), suggesting a possible origin for crossing dunes.

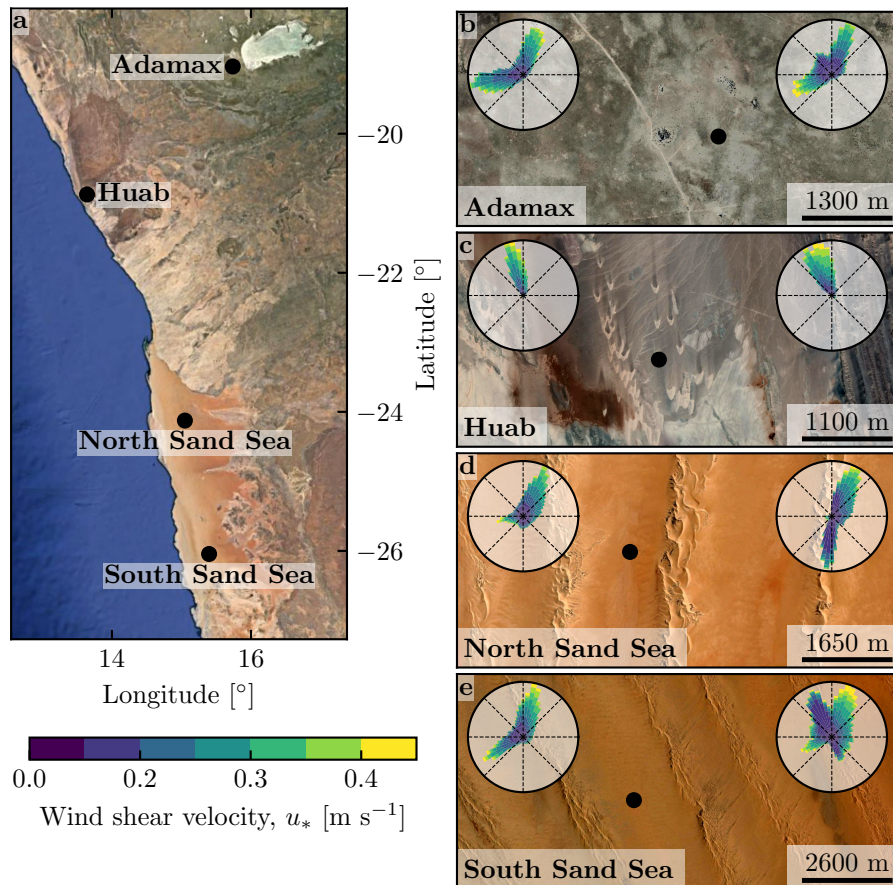


Fig. 1 Wind data used in this study **a**: Location of the different sites in Namibia. **b-e**: Satellite images of these different environments (Google-Earth, Maxar Technologies, CNES/Airbus). In each subplot, the left and right wind roses represent the data from the ERA5-Land climate reanalysis and the local wind stations, respectively. Note that the bars show the direction towards which the wind blows. The black dots show the location of local wind stations.

123 2 Wind regimes across the Namib Sand Sea

124 We have measured the wind regime in four different sites of at four different
 125 locations in Namibia, representative of various environments across and nearby
 126 arid environments across the Namib desert (Fig. 1, Online Resource Fig. S1).
 127 The Adamax station is located near the Adamax salt pan was located at
 128 the Adamax waterhole to the west of Etosha Pan in northern Namibia, in
 129 a highly sparsely vegetated area. The Huab station, on the coast at the
 130 outlet of the Huab river, is in an arid place where 60-m scale was near the
 131 coast on a hyper-arid flat gravel plain lying above the ephemeral Huab river.
 132 Here, 5–6 m high barchan dunes develop from the sediment blowing out

of the river valley. These two stations are were located in a relatively flat quantified how flat is flat environment environments. In contrast, the Deep North Sand Sea and South Namib stations are Sand Sea stations were located in the interdune between tens of meters high giant interdunes between 50–100 m high linear dunes with kilometer-scale wavelengths and superimposed patterns. In this section, we describe and compare winds from local measurements and climate reanalysis predictions.

2.1 Wind and elevation data

Local winds are measured at meteorological stations located in these four different places (black dots in At each meteorological station (Fig. 1). The wind strength and direction are , wind speed and direction were sampled every 10 minutes by using cup anemometers and wind vanes , at heights between 22 m and 33 m depending on the station. The available period of measurements ranges at each station ranged from 1 to 5 discontinuous years distributed between 2012 and 2020 (Suppl. Online Resource Fig. S1S2). We checked that at least one complete seasonal cycle is available at was available for each station. Regional winds are were extracted at the same locations and periods from the ERA5-Land dataset, which is a replay at a smaller spatial resolution of ERA5, the latest climate reanalysis from the ECMWF (Hersbach et al. 2020; Muñoz-Sabater et al. 2021). It provides This dataset provided hourly predictions of the 10-m wind velocity and direction at a spatial resolution of $0.1^\circ \times 0.1^\circ$ ($\simeq 9$ km in Namibia).

For To enable direct comparison, the local measurements are wind measurements were averaged into 1-hr bins centered on the temporal scale of the ERA5-Land estimates (Suppl. Online Resource Fig. S2S3). As the wind velocities of both datasets are were provided at different heights, we convert converted them into shear velocities (Suppl. Mat. u_* (Online Resource section 1), characteristic of the turbulent wind profile, which are then used together with the wind direction for further analysis. Wind roses in Fig. 1(b–e) show the resulting wind data.

Dune properties are were computed using autocorrelation on the 30-m Digital Elevation Models (DEMs) of the shuttle radar topography mission (Farr et al. 2007). For the South Namib and Deep Sand Sea and North Sand Sea stations, we obtain respectively, respectively, orientations of 85° and 125° with respect to the North, wavelengths of 2.6 km and 2.3 km and amplitudes (or half-heights) of 45 m and 20 m (Suppl. Online Resource Fig. S4 S5 for more details).

2.2 Comparison of local and regional winds

The obtained measured and predicted wind regimes are shown in figure 1. In the Namib, the regional wind patterns are essentially controlled by the see

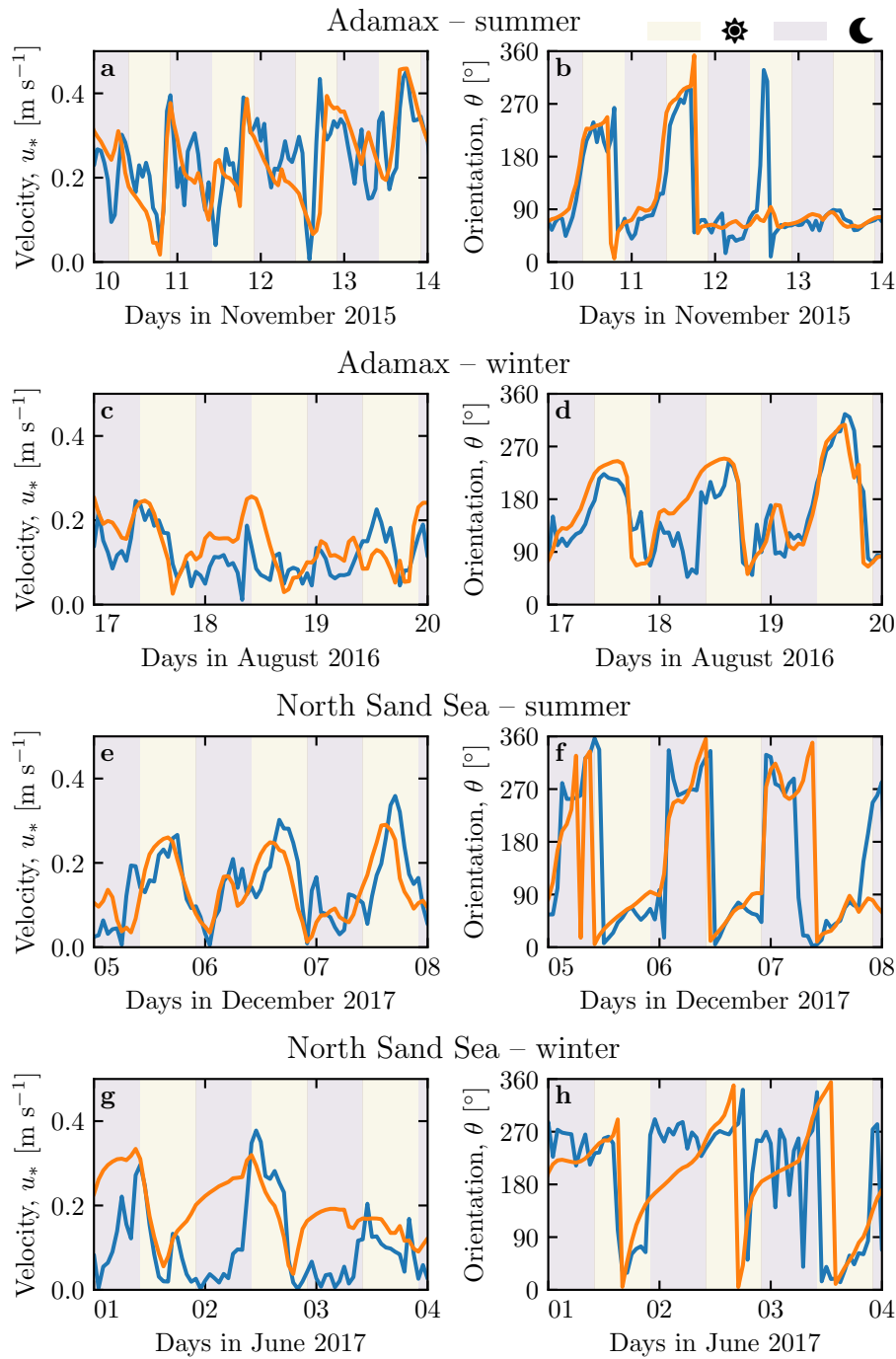


Fig. 2 Temporal comparison between the wind data coming from the ERA5-Land climate reanalysis (orange lines) and from the local measurements (blue lines). Coloured swathes indicate day (between 1000 UTC and 2200 UTC) and night (before 1000 UTC or after 2200 UTC). **a–b**: **Adamax** station in summer. **e–f**: **Deep-Sea-Adamax** station in winter. **e–f**: **Deep-North Sand** Sea station in summer. **g–h**: **North Sand Sea** station in winter. Time series of the two other stations are shown in Online Resource Fig. S6.

breeze, resulting in strong northward components (sometimes slightly deviated by the large scale topography ~~mountain?~~) present in all regional wind roses (Lancaster 1985). These daytime winds are dominant during the ~~second half of the year (September-January)~~. In winter period October-March (Fig. 2f and Online Resource Fig. S6f). During April-September, an additional easterly component can be recorded during the night, induced by the combination of katabatic winds forming in the mountains, and infrequent 'berg' winds, which are responsible ~~of for~~ the high wind velocities observed (Lancaster et al. 1984). The frequency of these easterly components decreases from ~~the~~-inland to the coast. As a result, bidirectional wind regimes within the Namib Sand Sea and at the Adamax salt pan (Fig. 1b,d,e) and a unidirectional wind regime on the coast at the outlet of the Huab River (Fig. 1c) are observed.

In the case of the Adamax and Huab stations, the time series of wind speed and direction from the regional predictions quantitatively match those corresponding to the local measurements (Fig. 2a,b) and Suppl. a-d and Online Resource Fig. S5-S6a-d, S7). For the Deep North Sand Sea and South Namib Sand Sea stations within the giant dune field, we observe that this agreement is also good, but limited to the ~~September-January~~ October-March time period (Fig. 2e,f-h and and Online Resource Fig. S6e-h). As a matter of fact, the measured wind roses exhibit additional wind components aligned with the giant dune orientation, as evidenced on the satellite images (Fig. 1c,d).

More precisely, during the ~~February-August~~ April-September period, the local and regional winds in the interdune match during daytime only, i.e when the southerly/southwesterly sea breeze dominates (Figs. 2(e,f) and 3, Suppl. Online Resource Fig. S6-S8). In the late afternoon and during the night, when the northwesterly 'berg' and katabatic winds blow, measurements and predictions differ. In this case, the angular wind distribution of the local measurements exhibits two additional modes corresponding to reversing winds aligned with the giant dune orientation (purple frame in Fig. 3, Suppl. Online Resource Figs. S6 and S7-S8 and S9). This deviation is also associated with a ~~global general~~ attenuation of the wind strength (Suppl. Online Resource Fig. S8-S10). Remarkably, all these figures show that ~~this these~~ wind reorientation and attenuation processes ~~typically occur occur only~~ at low wind velocities, typically for $u_* \lesssim 0.1 \text{ m s}^{-1}$. For shear velocities larger than $\simeq 0.25 \text{ m s}^{-1}$, the wind reorientation is not ~~significant apparent~~. Finally, for intermediate shear velocities, ~~moments of reorientation both situations of wind flow reoriented along the dune crest and others with no reorientation can both be observed~~ (Suppl. not reoriented can be successively observed (Online Resource Fig. S7). ~~CHECK the above lines cf. δu S9.~~

212 3 Influence of wind speed and circadian cycle on the atmospheric 213 boundary layer

214 The wind deflection induced by linear dunes has ~~so far mainly previously~~
215 been related to the incident angle between wind direction and crest orien-

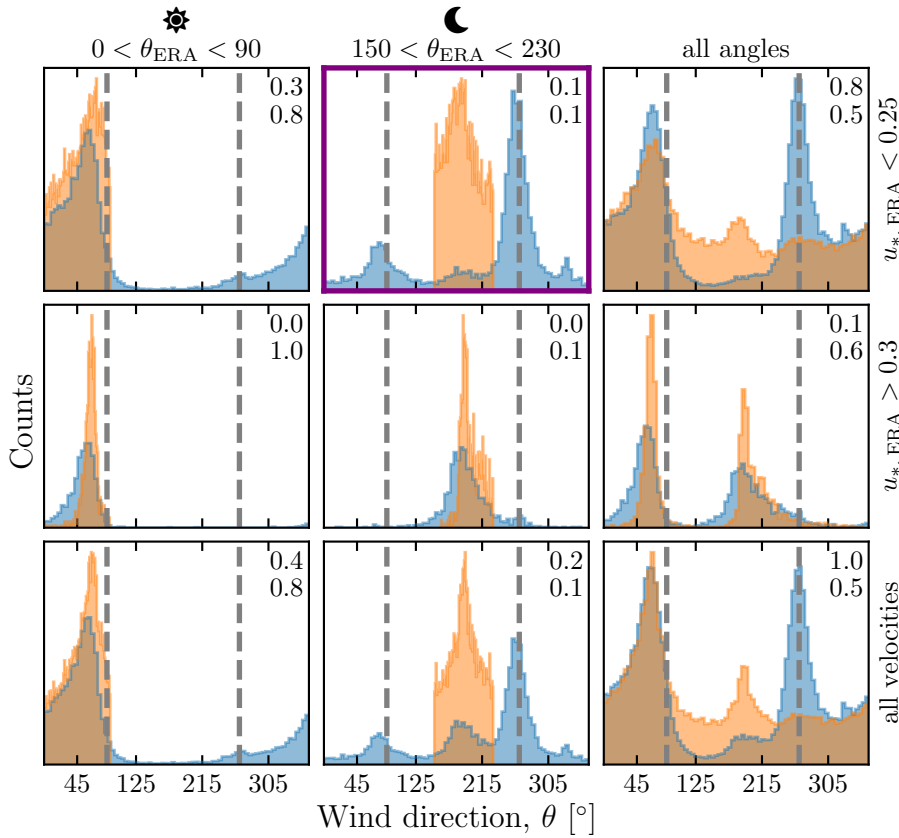


Fig. 3 Distributions of wind direction at the Deep North Sand Sea Station for the ERA5-Land climate reanalysis (orange) and the local measurements (blue). In each subplot, both distributions are plotted from the same time steps, selected with constraints on the wind direction (columns) and/or wind velocity (rows) of the ERA5-Land dataset. The gray vertical dashed lines indicate the dune orientation. The numbers at the top right give the percentage of time steps selected in each sub-range, as well as the percentage of them corresponding to the day daytime (between 1000 UTC and 2200 UTC). The purple frame highlights the regime (small low wind velocities, nocturnal summer easterly wind) in which the data from both datasets differ. A similar figure can be obtained for the Deep North Sand Sea station (Suppl. Online Resource Fig. S6S8).

tation, with a maximum deflection for evident for incident angles between 30° and 70° (Walker et al. 2009; Hesp et al. 2015). In the analysed data data analysed here, the most deflected wind at both Deep Sean and South Namib stations is the most the North and South Sand Sea stations is seen to be where the incident angle is perpendicular to the giant dunes (Fig. ??). The incident wind direction then does not seem to be the only parameter controlling the Figs. 1 and 3, Online Resource Fig. S8). It therefore appears that the incident wind angle is not the dominant control on maximum wind deflection. In contrast, a different behaviour is observed between low and high

wind velocities, suggesting Further, and as shown in Figure 3, winds of high and low velocities show contrasting behaviour in characteristics of deflection. This suggests a change in hydrodynamical regime between the winds. In this section, we discuss the relevant parameters associated with the dynamical mechanisms that govern the interactions between the atmospheric boundary layer flow and topographical obstacles giant dune topographies. This analysis allows us to provide a physics-based interpretation the observations of our measured wind data.

3.1 Flow over a modulated bed

Taking as a reference the turbulent flow over a flat bed, the general framework of this study is the understanding and the description of our study is understanding and describing the flow response to a bed modulation (e.g. a giant dune). Without loss of generality, we can consider in this context an idealised bed elevation in the form of parallel sinusoidal ridges, with wavelength λ (or wavenumber $k = 2\pi/\lambda$) and amplitude ξ_0 , and where the reference flow direction makes a given incident angle with respect to the ridge crest (Andreotti et al. 2012). Part of this response, on which we focus here, is the flow deflection by the ridges. In a simplified way, it can be understood from the Bernoulli principle (Hesp et al. 2015): as the flow approaches the ridge crest, the compression of the streamlines results in larger flow velocities, and thus lower pressures (Rubin and Hunter 1987). An incident flow oblique to the ridge is then deflected towards lower pressure zones, i.e. towards the crest. Turbulent dissipation tends to increase this effect downstream, resulting in wind deflection along the crest wind deflection in the lee side (Gadal et al. 2019).

Flow confinement below a capping surface, which enhances streamline compression, has a strong effect on the hydrodynamic response and typically increases flow deflection. This is the case for bedforms forming in open channel flows such as rivers (Fourrière et al. 2010; Unsworth et al. 2018). This is also relevant for aeolian dunes as they evolve in the turbulent atmospheric boundary layer (ABL) capped by the stratified free atmosphere (FA) (Andreotti et al. 2009). Two main mechanisms, associated with dimensionless numbers must then be considered (Fig. 4). First, topographic obstacles typically disturb the flow over a characteristic height similar to their length. As flow confinement is characterised by a thickness H , the interaction between the dunes and the wind in the ABL is well captured by the parameter kH . The height H is directly related to the radiative fluxes at the Earth surface. It is typically on the order of a kilometre, but significantly varies with the circadian and seasonal cycles. Emerging and small dunes, with wavelengths in the range 20 to 100 m, are not affected by the confinement, corresponding to $kH \gg 1$. For giant dunes with kilometric wavelengths, however, their interaction with the FA is significant (Andreotti et al. 2009). This translates into a parameter kH in the range 0.02–5, depending on the moment of the day and the season. A second important mechanism is associated with the

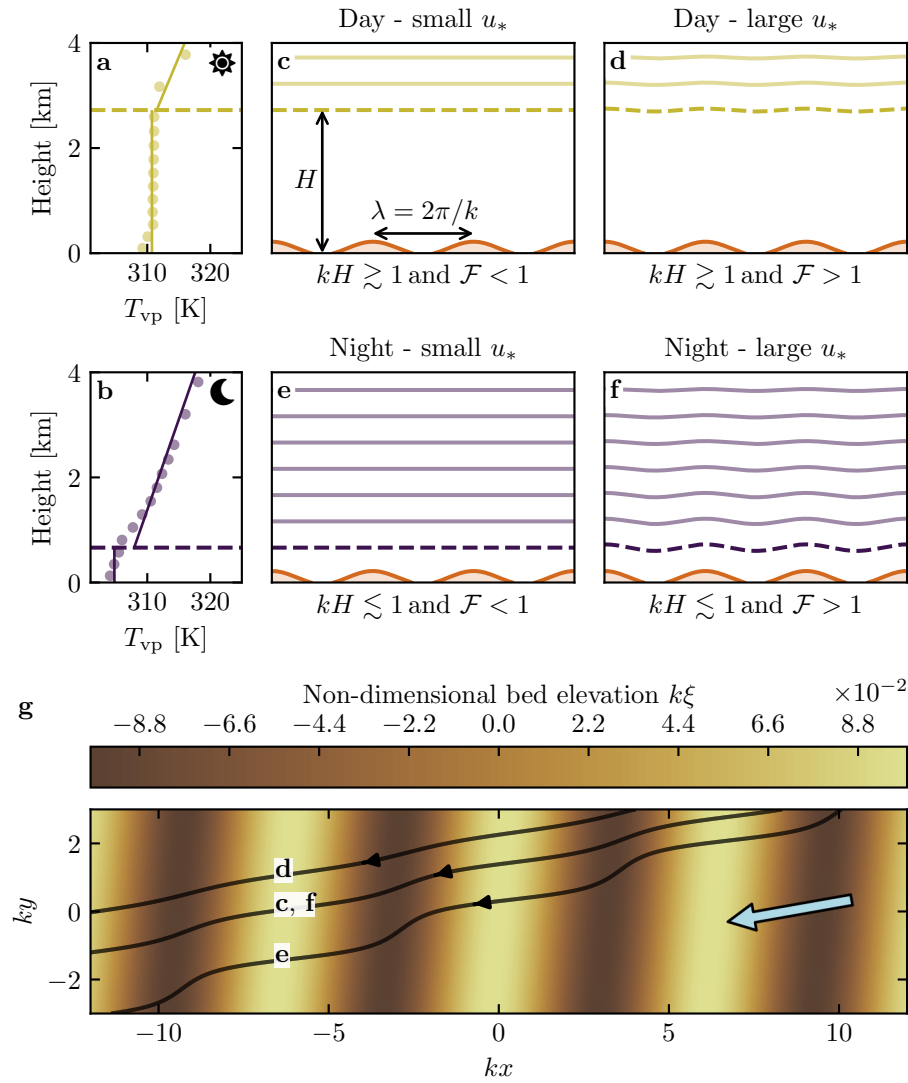


Fig. 4 a-ba-b: Vertical profiles of the virtual potential temperature at 2 different time steps (day - 03/11/2015 - 1200 UTC, night - 01/13/2013 - 0900 UTC) at the Deep North Sand Sea station. Dots: data from the ERA5 reanalysis. Dashed lines: boundary layer height given by the ERA5 reanalysis ([Suppl. Mat. Online Resource](#) section 2). Plain lines: vertical (boundary layer) and linear (free atmosphere) fits to estimate the stratification properties. **e-fc-f:** Sketches representing the interaction between the giant dunes and the atmospheric flow for different meteorological conditions. **g:** Streamlines over a sinusoidal topography $\xi(x, y)$ qualitatively representing the effect of low, medium and strong flow confinement, in relation to the above panels (see Appendix 1 for more details). [add arrow with reference wind](#) [The blue arrow indicates the undisturbed wind direction.](#)

268 existence of a thin intermediate so-called capping layer between the ABL and
 269 the FA. It is characterised by a density jump $\Delta\rho$, which controls the ‘rigidity’
 270 of this interface, i.e. how much its deformation affects streamline compression.
 271 This is usually quantified using the Froude number (Vosper 2004; Stull 2006;
 272 Sheridan and Vosper 2006; Hunt et al. 2006; Jiang 2014):

$$\mathcal{F} = \frac{U}{\sqrt{\frac{\Delta\rho}{\rho_0} g H}}, \quad (1)$$

273 where U is the wind velocity at the top of the ABL and ρ_0 its average density.
 274 The intensity of the stratification, i.e. the amplitude of the gradient $|\partial_z \rho|$, also
 275 ~~impact~~impacts its ability to deform the capping layer under the presence of an
 276 underlying obstacle, and thus affects the influence of flow confinement. This
 277 can be quantified using the internal Froude number (Vosper 2004; Stull 2006;
 278 Sheridan and Vosper 2006; Hunt et al. 2006; Jiang 2014) $\mathcal{F}_I = kU/N$, where
 279 $N = \sqrt{-g\partial_z \rho/\rho_0}$ is the the Brunt-Väisälä frequency (Stull 1988). Both Froude
 280 numbers have in practice the same qualitative effect on flow confinement, and
 281 we shall restrict the main discussion to \mathcal{F} only.

282 ~~This~~With this theoretical framework in mind, ~~and in the context of the~~measured wind data in the North and South Sand Sea stations, the small-
 283 est wind disturbances are expected to occur during the day, when the ABL
 284 depth is the largest and comparable to the dune wavelength ($kH \gtrsim 1$), which
 285 ~~correspond~~corresponds to a weak confinement situation (Fig. 4c,d). ~~On the~~On the contraryIn contrast, large wind disturbances are expected to occur during the
 286 night, when the confinement is mainly induced by a shallow ABL (Fig. 4e).
 287 However, this strong confinement can be somewhat reduced in the case of
 288 strong winds, corresponding to large values of the Froude number (Fig. 4f).
 289 This is in qualitative agreement with the transition from deflected to non-
 290 deflected winds related to low and high velocities observed in ~~the~~our data
 291 (Sec. 2.2).

294 3.2 Flow regime diagrams Data distribution in the flow regimes

295 We can go one step further and analyse how our data quantitatively spread over
 296 the different regimes discussed above. For that purpose, one needs to compute
 297 kH and \mathcal{F} from the time series. H , U and the other atmospheric parameters can be deduced from the various vertical profiles (temperature, humidity)
 298 available in the ERA5 climate reanalysis (~~Suppl. Mat.~~Online Resource section
 299 2). We quantify the flow deflection δ_θ as the minimal angle between the wind
 300 orientations comparing the local measurements and the regional predictions.
 301 We also compute the relative velocity modulation as

$$\delta_u = \frac{u_*^{\text{ERA}} - u_*^{\text{station}}}{u_*^{\text{ERA}}}. \quad (2)$$

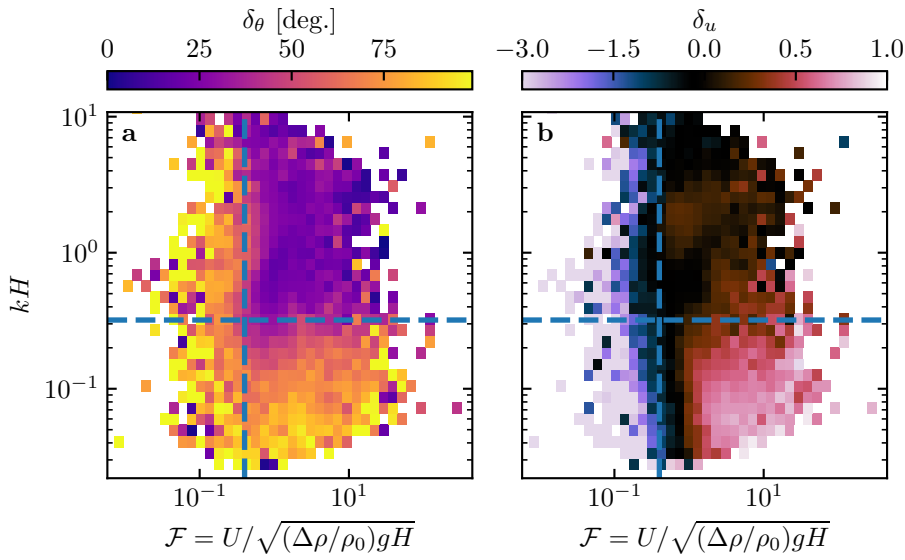


Fig. 5 Regime diagrams of the wind deviation δ_θ (a) and relative attenuation/amplification δ_u (b) in the space (\mathcal{F}, kH) , containing the data from both the Deep North Sand Sea and South Namib Sand Sea stations. Blue dashed lines empirically delimit the different regimes. The point density in each bin of the diagrams is shown in Suppl. Online Resource Fig. S11–S13 – 95% of the data occur in the range $-1 < \delta u < 1$. Similar regime diagrams in the spaces (\mathcal{F}_I, kH) and $(\mathcal{F}_I, \mathcal{F})$ are shown in Suppl. Online Resource Fig. S12–S14.

These two quantities are represented as maps in the plane (\mathcal{F}, kH) (Fig. 5a,b), and one can clearly identify different regions in these graphs. Small wind disturbances (small δ_θ and δ_u) are located in the top-right part of the diagrams, corresponding to a regime with low-interaction as well as low-confinement (kH and \mathcal{F} large enough, Fig. 4d). Lower values of kH (stronger interaction) or of Froude number (stronger confinement) both lead to an increase in wind disturbances, both in terms of orientation and velocity. Below a crossover value $kH \simeq 0.3$, wind disturbance is less sensitive to the \mathcal{F} -value. This is probably due to enhanced non-linear effects linked to strong flow modulation by the obstacle when confinement is strong. The Froude number also controls a transition from damped to amplified wind velocities in the interdune, with a crossover around $\mathcal{F} \simeq 0.4$ (Fig. 5b). Such an amplification is rather unexpected. Checking the occurrence of the corresponding data, it appears that they are mainly associated with the wind coming from the South, when it blows southerly sea breeze, and occur dominantly during the October–March period, when the other easterly wind is not present (Online Resource Fig. S15a–b). Furthermore, they occur less frequently during the afternoon, and more frequently at the end of day, but in summer time only although it is also present in winter (an additional suppl. fig. ?the day (Online Resource Fig. S15c)). This effect may be linked to a change in the flow behaviour in the lee side of the obstacle (lee

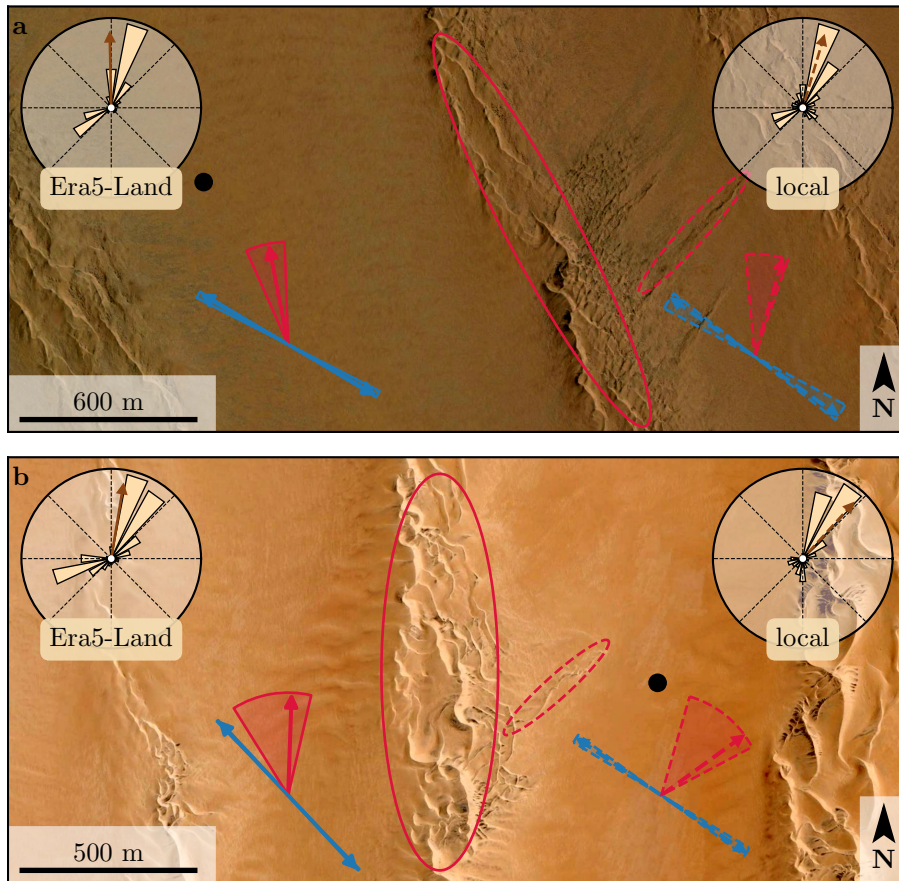


Fig. 6 Implications for smaller scale patterns in (a) the South [Namib Sand Sea](#) and (b) [Deep North Sand Sea](#). The ellipses indicate the different types of elongating dunes, at large (plain line) and small (dashed line) scales. Dune orientation are predicted using the model of Courrech du Pont et al. (2014) from the sand flux angular distributions, shown here (roses and resultant transport direction) for typical values (grain size $180 \mu\text{m}$, flux-up ratio of 1.6). Code for corresponding arrows: use of ERA5-Land data (plain line), use of local measurements (dashed line), prediction for the bed instability growth mechanism (blue), prediction for the elongation growth mechanism (red). Wedges show the uncertainty on the orientation calculation when parameters are varied. The black dots indicate the location of the meteorological stations with respect to the dunes. See Appendix 2 for additional details.

324 [waves, hydraulic jumps, rotors](#)) [obstacles](#) but further measurements are clearly
 325 needed in order to assess the different possibilities (Baines 1995; Vosper 2004).

326 4 Discussion and conclusion

327 The [feedback of the giant dunes on the wind flow has important implications](#)
 328 [for smaller scales bedforms. As illustrated in Fig. 6, small linear dunes \(\$\sim 50 \text{ m}\$](#)

-wide) are often present in the 1–2 km interdune between giant linear dunes in the Namib Sand Sea. These smaller dunes do not exhibit the same orientation as the large ones, and are sometimes considered to be ‘crossing dunes’. Whilst differences between large and small scale dune patterns are observed ubiquitously, they are largely attributed to the presence of two different dune growth mechanisms, leading to two different dune patterns (orientations and/or morphologies) for the same wind regime (Courrech du Pont et al. 2014; Runyon et al. 2017; Lü et al. 2017; Song et al. 2019; Gadal et al. 2020). Here, however, our arguments enable the development of differing orientations for the small and giant linear dunes whilst also imposing the same dune growth mechanism (elongating mode). Figure 6 shows how the orientations for the small and giant dunes can be derived from the locally measured and regionally predicted winds respectively (red arrows in Fig. 6). The feedback of the giant dunes on the wind described in this study thus provides an explanation for the existence of these small linear dunes elongating across the interdune, a dynamic which has remained unresolved to date. Further studies are of course needed to confirm this hypothesis. These crossing dunes could provide additional constraints for the inference of local winds from bedforms, similarly to what is currently performed on Mars using ripple orientations (Liu and Zimbelman 2015; Hood et al. 2021).

Also, this study highlights the interaction between giant dunes and the atmospheric boundary layer. It thus supports the still debated idea that the capping layer acts as a bounding surface impacting the dune dynamics, and limiting dune growth in particular (Andreotti et al. 2009), in contrast to an unconstrained growth ever-slower with size (Eastwood et al. 2011; Gunn et al. 2021). Interestingly, this mechanism would allow for the inference of the ABL depth from the giant bedforms spacing where measurements are not feasible or available, as e.g. performed by Lorenz et al. (2010) on Titan.

To sum up conditions under which the ERA5-Land reanalysis data can reliably be used to study dune morphodynamics, we summarise the comparison of local (direct measurements) and regional (climate reanalysis) wind data ~~reveals the giant dune feedback on the wind flow~~. In flat areas, the agreement between the two confirms the ability of the ERA5-Land climate reanalysis to predict the wind regime down to scales ~ 10 km, i.e the model grid. When smaller scale topographies are present (giant dunes in our case), locally measured winds can significantly differ from the regionally predicted ones. This is the case when the disturbances induced by the dunes interact with the lower part of the ABL vertical structure, which presents circadian variations. During the day, when the capping layer is typically high, this interaction is small, and the ERA5-Land predictions are also quantitatively consistent with the local data. During the night, however, the presence of a shallow atmospheric boundary layer induces a strong confinement of the flow, and is associated with large wind deflection by the dunes. Importantly, we find that this effect can be counterbalanced for large wind velocities, which are capable of deforming the capping layer, thus decreasing the influence of the confinement.

The theoretical computation of the wind disturbances induced by sinusoidal ridges under flow confinement has been performed in the linear limit

(?Andreotti et al. 2012) (Andreotti et al. 2009, 2012), i.e. when the aspect ratio of these ridges is small ($k\xi_0 \ll 1$). These models are able to qualitatively reproduce the observed wind deflection (Appendix 1, Suppl. Online Resource Figs. S12 and S13S14 and S16), and thus provide the physical support for the hydrodynamic picture interpretation we propose here. They however cannot reach based on hydrodynamic regimes. However, these models cannot quantitatively predict the magnitude of these observations, probably due to the presence of expected non-linearities in high confinement situations linked to strong flow modulations. Besides, these linear calculations only predict wind attenuation in the interdune, in contrast with the observed enhanced velocities associated with particular summer evening winds from the South during the period October–March (Online Resource Fig. S15). Some other models also predict different spatial flow structures in response to a modulated topography, such as lee waves and rotors (Baines 1995; Vosper 2004), which of course (Baines 1995; Vosper 2004). Of course they cannot be observed by our single point measurements located at a single point in the interdune. Data at different places along and across the ridges are needed to investigate and possibly map such flow structures, and for further comparisons with the models.

This study highlights the interaction between giant dunes and the atmospheric boundary layer. It then supports the debated idea that the capping layer acts as a bounding surface impacting the dune dynamics, and limiting dune growth in particular (?), as opposed to an unconstrained growth ever slower with size (Eastwood et al. 2011; Gunn et al. 2021). Interestingly, this mechanism would allow for the inference of the ABL depth from the giant bedforms spacing where measurements are not feasible or available, as e.g. performed by Lorenz et al. (2010) on Titan.

This interaction also has important implications for smaller scales bedforms, as illustrated in Fig. 6. In the Namib Sand Sea, small linear dunes (~ 50 m wide) are present in the interdune between giant linear dunes (~ 2 km wide). Strangely enough, the small dunes do not have the same orientation as the large ones, and sometimes denotes as ‘crossing dunes’. While differences between large and small scale dune patterns are observed ubiquitously, they are now largely attributed to the presence of two different dune growth mechanisms, leading to two different dune patterns (orientations and/or morphologies) for the same wind regime (Courrech du Pont et al. 2014; Runyon et al. 2017; Lü et al. 2017; Song et al. 2019; Gadal et al. 2021). Here, however, we can get the orientations of the small and giant linear dunes from the same dune growth mechanism (elongating mode), respectively using the locally measured and regionally predicted winds (red arrows in Fig. 6). The feedback of the giant dunes on the wind described in this study then provides an explanation for the existence of these small linear dunes elongating across the interdune, as yet unresolved. Further studies are of course needed to confirm this hypothesis. These crossing dunes could provide additional constraints for the inference of local winds from bedforms, similarly to what is currently performed on Mars using ripple orientations (Liu and Zimbelman 2015; Hood et al. 2021).

421 **Acknowledgements** We would like to acknowledge the contributors of the following open-
 422 source python librairies, Matplotlib (Hunter 2007), Numpy (Harris et al. 2020) and Scipy
 423 (Virtanen et al. 2020), which provide an incredibly efficient ecosystem allowing scientific
 424 research in Python.

425 ERA5 and ERA5-Land datasets are publicly available at the Copernicus Climate Change
 426 Service (C3S) Climate Data Store. The locally measured wind data can be found at [up-](#)
 427 [load on public data repository](#). The digital elevation models from the Shuttle Radar To-
 428 graphy Mission are publicly available from Nasa servers, and can be downloaded at
 429 <https://dwtkns.com/srtm30m/>. Fully documented codes used to analyse this study are
 430 available at <https://github.com/Cgadal/GiantDunes> (will be made public upon acceptance
 431 of this manuscript for publication).

432 [citing all [relevant](#) grants ...] [TOAD](#)

433 **Appendix 1: Linear theory of wind response to topographic pertur-
 434 bation**

435 Following the work of Fourrière et al. (2010), Andreotti et al. (2012) and
 436 [?Andreotti et al. \(2009\)](#), we briefly [expose](#)-[describe](#) in this appendix the frame-
 437 [ef](#)-[for](#) the linear response of a turbulent flow to a topographic perturba-
 438 tion of small aspect ratio. As a general bed elevation can be decomposed into
 439 Fourier modes, we focus here on a sinusoidal topography:

$$\xi = \xi_0 \cos \left[k \left(\cos(\alpha) \underline{x} + \underline{y} - \sin(\alpha) \underline{y} \underline{x} \right) \right], \quad (3)$$

440 which is also a good approximation for the giant dunes observed in the [Deep](#)
 441 [North Sand Sea](#) and [South Namib Sand Sea](#) Station (Fig. 1 and [Suppl.-Online](#)
 442 [Resource](#) Fig. [S4](#)-[S5](#)). [Here](#), x and y are the streamwise and spanwise co-
 443 ordinates, $k = 2\pi/\lambda$ the wavenumber of the sinusoidal perturbation, [and](#)- α
 444 its crest orientation with respect to the $\underline{y} \underline{x}$ -direction ([anticlockwise](#)) and ξ_0 its
 445 [amplitude](#). The two components of the basal shear stress $\tau = \rho_0 u_* \mathbf{u}_*$, constant
 446 in the flat bottom reference case, can then be generically written as:

$$\tau_x = \tau_0 \left(1 + k \xi_0 \sqrt{\mathcal{A}_x^2 + \mathcal{B}_x^2} \cos \left[k \left(\cos(\alpha) \underline{x} + \underline{y} - \sin(\alpha) \underline{y} \underline{x} \right) + \phi_x \right] \right), \quad (4)$$

$$\tau_y = \tau_0 k \xi_0 \sqrt{\mathcal{A}_y^2 + \mathcal{B}_y^2} \cos \left[k \left(\cos(\alpha) \underline{x} + \underline{y} - \sin(\alpha) \underline{y} \underline{x} \right) + \phi_y \right], \quad (5)$$

447 where τ_0 is the reference basal shear stress on a flat bed. We have defined
 448 the phase $\phi_{x,y} = \tan^{-1}(\mathcal{B}_{x,y}/\mathcal{A}_{x,y})$ from the in-phase and in-quadrature hy-
 449 drodynamical coefficients $\mathcal{A}_{x,y}$ and $\mathcal{B}_{x,y}$. They are functions of k and of the
 450 flow conditions, i.e the bottom roughness, the vertical flow structure and the
 451 incident flow direction, and the theoretical framework developed in the above
 452 cited papers proposes methods to compute them in the linear regime.

Following Andreotti et al. (2012), the effect of the incident wind direction can be approximated by the following expressions:

$$\mathcal{A}_x = \mathcal{A}_0 \cos \alpha \sin^2 \alpha, \quad (6)$$

$$\mathcal{B}_x = \mathcal{B}_0 \cos \alpha \sin^2 \alpha, \quad (7)$$

$$\mathcal{A}_y = -\frac{1}{2} \mathcal{A}_0 \cos \alpha \sin \alpha, \quad (8)$$

$$\mathcal{B}_y = -\frac{1}{2} \mathcal{B}_0 \cos \alpha \sin \alpha, \quad (9)$$

where \mathcal{A}_0 and \mathcal{B}_0 are now two coefficients independent of the dune orientation α , corresponding to the transverse case ($\alpha = 90^\circ$). For a fully turbulent boundary layer capped by a stratified atmosphere, these coefficients depend on kH , kz_0 , \mathcal{F} and \mathcal{F}_1 (Andreotti et al. 2009). In this study, we assume a constant hydrodynamic roughness $z_0 \simeq 1$ mm (Suppl. Mat. Online Resource section 1). For the considered giant dunes, this leads to $kz_0 \simeq 2 \cdot 10^{-6}$, as their wavelength is $\lambda \simeq 2.4$ km (or $k \simeq 2 \cdot 10^{-3} \text{ m}^{-1}$). Values of z_0 extracted from field data indeed typically fall between 0.1 mm and 10 mm (Sherman and Farrell 2008; Field and Pelletier 2018). Importantly, \mathcal{A}_0 and \mathcal{B}_0 do not vary much in the corresponding range of kz_0 (Fourrière et al. 2010), and the results presented here are robust with respect to this choice.

With capping α -layer height and Froude numbers computed from the ERA5-Land time series, the corresponding \mathcal{A}_0 and \mathcal{B}_0 can be deduced, allowing to produce maps as displayed in Suppl. Online Resource Fig. S13S16. Interestingly, it shows similar regimes as in the diagrams of Fig. 5 and Online Resource Fig. S12S14a,b, supporting the physics picture. However, the matching remains qualitative only. As a matter of fact, the linearity assumption of the theoretical framework requires $(|\tau| - \tau_0) / \tau_0 \ll 1$, which translates into $k\xi \sqrt{\mathcal{A}_0^2 + \mathcal{B}_0^2} \ll 1$. In our case, the giant dune morphology gives $k\xi_0 \simeq 0.1$, which means that one quits the regime of validity of the linear theory when the coefficient modulus $\sqrt{\mathcal{A}_0^2 + \mathcal{B}_0^2}$ becomes larger than a few units. In accordance with the theoretical expectations, these coefficients present values on the order of unity ($\mathcal{A}_0 \simeq 3$ and $\mathcal{B}_0 \simeq 1$) in unconfined situations (Claudin et al. 2013; Lü et al. 2021). In contrast and as illustrated in Suppl. Online Resource Fig. S12S16a,b, larger values are predicted in case of strong confinement, which does not allow us to proceed to further quantitative comparison with the data.

Finally, the linear model is also able to reproduce the enhancement of the flow deflection over the sinusoidal ridges when $\sqrt{\mathcal{A}_0^2 + \mathcal{B}_0^2}$ is increased (Suppl. Online Resource Fig. S13S16). Here, using $k\xi_0 \simeq 0.1$ to be representative of the amplitude of the giant dunes at the Deep North Sand Sea station, the coefficient modulus is bounded to 10.

487 Appendix 2: Sediment transport and dune morphodynamics

488 We summarise in this appendix the sediment transport and dune morphodynamics
 489 theoretical framework leading to the prediction of sand fluxes and dune
 490 orientations from wind data.

491 *Sediment transport* — The prediction of sand fluxes from wind data has been
 492 a long standing issue in aeolian geomorphological studies (Fryberger and Dean
 493 1979; Pearce and Walker 2005; Sherman and Li 2012; Shen et al. 2019). Based
 494 on laboratory studies in wind tunnels (Rasmussen et al. 1996; Iversen and
 495 Rasmussen 1999; Creyssels et al. 2009; Ho et al. 2011), as well as physical
 496 considerations (Ungar and Haff 1987; Andreotti 2004; Durán et al. 2011; Pähzt
 497 and Durán 2020), it has been shown that the steady saturated saltation flux
 498 over a flat sand bed depends linearly on the shear stress:

$$\frac{q_{\text{sat}}}{Q} = \Omega \sqrt{\Theta_{\text{th}}} (\Theta - \Theta_{\text{th}}), \quad (10)$$

499 where Ω is a proportionality constant, $Q = d\sqrt{(\rho_s - \rho_0)gd/\rho_0}$ is a character-
 500 istic flux, $\Theta = \rho_0 u_*^2 / (\rho_s - \rho_0)gd$ the Shields number, and Θ_{th} its threshold
 501 value below which saltation vanishes. $\rho_s = 2.6 \text{ g cm}^{-3}$ and $d = 180 \mu\text{m}$ are
 502 the grain density and diameter, and g is the gravitational acceleration. The
 503 shear velocity, and consequently the Shields number as well as the sediment
 504 flux, are time dependent.

505 Recently, Pähzt and Durán (2020) suggested an additional quadratic term
 506 in Shields to account for grain-grain interactions within the transport layer at
 507 strong wind velocities:

$$\frac{q_{\text{sat}, t}}{Q} = \frac{2\sqrt{\Theta_{\text{th}}}}{\kappa\mu} (\Theta - \Theta_{\text{th}}) \left(1 + \frac{C_M}{\mu} [\Theta - \Theta_{\text{th}}] \right), \quad (11)$$

508 where $\kappa = 0.4$ is the von Kármán constant, $C_M \simeq 1.7$ a constant and $\mu \simeq 0.6$ is
 509 a friction coefficient, taken to be the avalanche slope of the granular material.
 510 The fit of this law to the experimental data of Creyssels et al. (2009) and Ho
 511 et al. (2011) gives $\Theta_{\text{th}} = 0.0035$. The fit of Eq. 10 on these same data similarly
 512 gives $\Omega \simeq 8$ and $\Theta_{\text{th}} = 0.005$. The sand flux angular distributions and the
 513 dune orientations in Fig. 6 are calculated using this law (11). We have checked
 514 that using the ordinary linear relationship (10) instead does not change the
 515 predicted dune orientations by more than a few degrees.

516 *Dune orientations* — Dune orientations are predicted with the dimensional
 517 model of Courrech du Pont et al. (2014), from the sand flux time series com-
 518 puted with the above transport law. Two orientations are possible depending
 519 on the mechanism dominating the dune growth: elongation or bed instabil-
 520 ity. The orientation α corresponding the bed instability is then the one that
 521 maximises the following growth rate (Rubin and Hunter 1987):

$$\sigma \propto \frac{1}{H_d W_d T} \int_0^T q_{\text{crest}} |\sin(\theta - \alpha)| dt, \quad (12)$$

522 where θ is the wind orientation measured with respect to the same reference
 523 as α , and H_d and W_d are dimensional constants respectively representing the
 524 dune height and width. The integral runs over a time T , which must be repre-
 525 sentative of the characteristic period of the wind regime. The flux at the crest
 526 is expressed as:

$$q_{\text{crest}} = q_{\text{sat}} [1 + \gamma |\sin(\theta - \alpha)|], \quad (13)$$

527 where the flux-up ratio γ has been calibrated to 1.6 using field studies, under-
 528 water laboratory experiments and numerical simulations. Predictions of the
 529 linear analysis of Gadal et al. (2019) [and Delorme et al. \(2020\)](#) give similar
 530 results.

531 Similarly, the dune orientation corresponding to the elongation mechanism
 532 is the one that verifies:

$$\tan(\alpha) = \frac{\langle q_{\text{crest}}(\alpha) \mathbf{e}_\theta \rangle \cdot \mathbf{e}_{WE}}{\langle q_{\text{crest}}(\alpha) \mathbf{e}_\theta \rangle \cdot \mathbf{e}_{SN}}, \quad (14)$$

533 where $\langle \cdot \rangle$ denotes a vectorial time average. The unitary vectors \mathbf{e}_{WE} , \mathbf{e}_{SN} and
 534 \mathbf{e}_θ are in the West-East, South-North and wind directions, respectively.

535 The resulting computed dune orientations, blue and red arrows in Fig. 6,
 536 then depend on a certain number of parameters (grain properties, flux-up
 537 ratio, etc.), for which we take typical values for aeolian sandy deserts. Due
 538 to the lack of measurements in the studied places, some uncertainties can
 539 be expected. We therefore run a [sensitivity sensitivity](#) test by calculating the
 540 dune orientations for grain diameters ranging from 100 μm to 400 μm and for
 541 a speed-up ratio between 0.1 and 10 (wedges in Fig. 6).

542 References

- 543 Andreotti B (2004) A two-species model of aeolian sand transport. *J Fluid
544 Mech* 510:47–70
- 545 Andreotti B, Fourrière A, Ould-Kaddour F, Murray B, Claudin P (2009) Gi-
546 ant aeolian dune size determined by the average depth of the atmospheric
547 boundary layer. *Nature* 457:1120–1123
- 548 Andreotti B, Claudin P, Devauchelle O, Durán O, Fourrière A (2012) Bedforms
549 in a turbulent stream: ripples, chevrons and antidunes. *J Fluid Mech* 690:94–
550 128
- 551 Ashkenazy Y, Yizhaq H, Tsoar H (2012) Sand dune mobility under climate
552 change in the kalahari and australian deserts. *Climatic Change* 112:901–923
- 553 Baddock M, Livingstone I, Wiggs G (2007) The geomorphological significance
554 of airflow patterns in transverse dune interdunes. *Geomorphology* 87:322–
555 336
- 556 Baines PG (1995) Topographic effects in stratified flows. Cambridge university
557 press
- 558 Bauer BO, Sherman DJ, Wolcott JF (1992) Sources of uncertainty in shear
559 stress and roughness length estimates derived from velocity profiles. *Prof
560 Geogr* 44:453–464
- 561 Belcher S, JCR H (1998) Turbulent flow over hills and waves. *Annu Rev Fluid
562 Mech* 30:507–538
- 563 Blumberg DG, Greeley R (1996) A comparison of general circulation model
564 predictions to sand drift and dune orientations. *J Clim* 9:3248–3259
- 565 Bristow NR, Best J, Wiggs GFS, Nield JM, Baddock MC, Delorme P, Chris-
566 tensen KT (2022) Topographic perturbation of turbulent boundary layers
567 by low-angle, early-stage aeolian dunes. *Earth Surface Processes and Land-
568 forms* n/a(n/a), DOI <https://doi.org/10.1002/esp.5326>
- 569 Brown S, Nickling WG, Gillies JA (2008) A wind tunnel examination of shear
570 stress partitioning for an assortment of surface roughness distributions. *J
571 Geophys Res* 113:F02S06
- 572 Charru F, Andreotti B, Claudin P (2013) Sand ripples and dunes. *Annu Rev
573 Fluid Mech* 45:469–493
- 574 Claudin P, Wiggs G, Andreotti B (2013) Field evidence for the upwind velocity
575 shift at the crest of low dunes. *Boundary-layer Meteorol* 148:195–206
- 576 Claudin P, Durán O, Andreotti B (2017) Dissolution instability and roughen-
577 ing transition. *J Fluid Mech* 832:R2
- 578 Claudin P, Louge M, Andreotti B (2021) Basal pressure variations induced by
579 a turbulent flow over a wavy surface. *Front Phys* 9:682,564
- 580 Courrech du Pont S (2015) Dune morphodynamics. *C R Physique* 16:118–138
- 581 Courrech du Pont S, Narteau C, Gao X (2014) Two modes for dune orientation.
582 *Geology* 42:743–746
- 583 Creyssels M, Dupont P, El Mohtar AO, Valance A, Cantat I, Jenkins JT, Pasini
584 JM, Rasmussen KR (2009) Saltating particles in a turbulent boundary layer:
585 experiment and theory. *J Fluid Mech* 625:47–74

- 586 Dee DP, Uppala SM, Simmons AJ, Berrisford P, Poli P, Kobayashi S, Andrae
587 U, Balmaseda M, Balsamo G, Bauer dP, et al. (2011) The era-interim re-
588 analysis: Configuration and performance of the data assimilation system. *Q*
589 *J R Meteorol Soc* 137:553–597
- 590 Delorme P, Wiggs G, Baddock M, Claudin P, Nield J, Valdez A (2020) Dune
591 initiation in a bimodal wind regime. *J Geophys Res* 125:e2020JF005,757
- 592 Durán O, Claudin P, Andreotti B (2011) On aeolian transport: Grain-scale
593 interactions, dynamical mechanisms and scaling laws. *Aeolian Res* 3:243–
594 270
- 595 Durran DR (1990) Mountain waves and downslope winds. In: *Atmospheric*
596 *processes over complex terrain*, Springer, pp 59–81
- 597 Eastwood E, Nield J, Baas A, Kocurek G (2011) Modelling controls on aeolian
598 dune-field pattern evolution. *Sedimentology* 58:1391–1406
- 599 Farr TG, Rosen PA, Caro E, Crippen R, Duren R, Hensley S, Kobrick M,
600 Paller M, Rodriguez E, Roth L, et al. (2007) The shuttle radar topography
601 mission. *Rev Geophys* 45
- 602 Fernando H, Mann J, Palma J, Lundquist JK, Barthelmie RJ, Belo-Pereira M,
603 Brown W, Chow F, Gerz T, Hocut C, et al. (2019) The perdigão: Peering
604 into microscale details of mountain winds. *Bull Amer Meteor Soc* 100:799–
605 819
- 606 Field JP, Pelletier JD (2018) Controls on the aerodynamic roughness length
607 and the grain-size dependence of aeolian sediment transport. *Earth Surf*
608 *Process Landforms* 43:2616–2626
- 609 Finnigan J, Raupach M, Bradley E, Aldis G (1990) A wind tunnel study
610 of turbulent flow over a two-dimensional ridge. *Boundary-layer Meteorol*
611 50:277–317
- 612 Finnigan J, Ayotte K, Harman I, Katul G, Oldroyd H, Patton E, Poggi D,
613 Ross A, Taylor P (2020) Boundary-layer flow over complex topography.
614 *Boundary-layer Meteorol* 177:247–313
- 615 Flack K, Schultz M (2010) Review of hydraulic roughness scales in the fully
616 rough regime. *J Fluids Eng* 132:041,203
- 617 Fourrière A, Claudin P, Andreotti B (2010) Bedforms in a turbulent stream:
618 formation of ripples by primary linear instability and of dunes by nonlinear
619 pattern coarsening. *J Fluid Mech* 649:287–328
- 620 Frederick KA, Hanratty TJ (1988) Velocity measurements for a turbulent non-
621 separated flow over solid waves. *Exp Fluids* 6:477–486
- 622 Fryberger SG, Dean G (1979) Dune forms and wind regime. A study of global
623 sand seas 1052:137–169
- 624 Gadal C, Narteau C, Courrech Du Pont S, Rozier O, Claudin P (2019) Incip-
625 ient bedforms in a bidirectional wind regime. *J Fluid Mech* 862:490–516
- 626 Gadal C, Narteau C, Courrech du Pont S, Rozier O, Claudin P (2020) Peri-
627 odicity in fields of elongating dunes. *Geology* 48:343–347
- 628 Gong W, Ibbetson A (1989) A wind tunnel study of turbulent flow over model
629 hills. *Boundary-layer Meteorol* 49:113–148
- 630 Gong W, Taylor P, Dörnbrack A (1996) Turbulent boundary-layer flow over
631 fixed aerodynamically rough two-dimensional sinusoidal waves. *J Fluid Mech*

- 632 312:1–37
- 633 Gunn A, Wanker M, Lancaster N, Edmonds D, Ewing R, Jerolmack
634 D (2021) Circadian rhythm of dune-field activity. *Geophys Res Lett*
635 48:e2020GL090,924
- 636 Harris CR, Millman KJ, van der Walt SJ, Gommers R, Virtanen P, Cournau-
637 peau D, Wieser E, Taylor J, Berg S, Smith NJ, et al. (2020) Array program-
638 ming with numpy. *Nature* 585:357–362
- 639 Hersbach H, Bell B, Berrisford P, Hirahara S, Horányi A, Muñoz-Sabater J,
640 Nicolas J, Peubey C, Radu R, Schepers D, et al. (2020) The era5 global
641 reanalysis. *Q J R Meteorol Soc* 146:1999–2049
- 642 Hesp PA, Smyth TAG, Nielsen P, Walker IJ, Bauer BO, Davidson-Arnott R
643 (2015) Flow deflection over a foredune. *Geomorphology* 230:64–74
- 644 Ho TD, Valance A, Dupont P, Ould El Moctar A, Tuan Duc H, Valance A,
645 Dupont P, Ould El Moctar A (2011) Scaling laws in aeolian sand transport.
646 *Phys Rev Lett* 106:4–7
- 647 Hood DR, Ewing RC, Roback KP, Runyon K, Avouac JP, McEnroe M (2021)
648 Inferring airflow across martian dunes from ripple patterns and dynamics.
649 *Front Earth Sci* 9:702,828
- 650 Howard AD (1977) Effect of slope on the threshold of motion and its applica-
651 tion to orientation of wind ripples. *Geol Soc Am Bull* 88:853–856
- 652 Hu Z, Gao X, Lei J, Zhou N (2021) Geomorphology of aeolian dunes in the
653 western sahara desert. *Geomorphology* 392:107,916
- 654 Hunt J, Leibovich S, Richards K (1988) Turbulent shear flows over low hills.
655 *Q J R Meteorol Soc* 114:1435–1470
- 656 Hunt JCR, Vilenski GG, Johnson ER (2006) Stratified separated flow around
657 a mountain with an inversion layer below the mountain top. *J Fluid Mech*
658 556:105–119
- 659 Hunter JD (2007) Matplotlib: A 2d graphics environment. *Computing in sci-
660 ence & engineering* 9:90–95
- 661 Iversen JD, Rasmussen KR (1999) The effect of wind speed and bed slope on
662 sand transport. *Sedimentology* 46:723–731
- 663 Jackson PS, Hunt JCR (1975) Turbulent wind flow over a low hill. *Q J R
664 Meteorol Soc* 101:929–955
- 665 Jiang Q (2014) Applicability of reduced-gravity shallow-water theory to atmo-
666 spheric flow over topography. *J Atmos Sci* 71:1460–1479
- 667 Jolivet M, Braucher R, Dovchintseren D, Hocquet S, Schmitt J, ASTER Team
668 (2021) Erosion around a large-scale topographic high in a semi-arid sedimen-
669 tary basin: Interactions between fluvial erosion, aeolian erosion and aeolian
670 transport. *Geomorphology* 386:107,747
- 671 Kim HG, Patel VC, Lee CM (2000) Numerical simulation of wind flow
672 over hilly terrain. *Journal of wind engineering and industrial aerodynamics*
673 87:45–60
- 674 Lancaster J, Lancaster N, Seely M (1984) Climate of the central namib desert.
675 Madoqua 1984:5–61
- 676 Lancaster N (1985) Winds and sand movements in the namib sand sea. *Earth
677 Surf Process Landforms* 10:607–619

- 678 Lewis HW, Mobbs SD, Lehning M (2008) Observations of cross-ridge flows
679 across steep terrain. *Q J R Meteorol Soc* 134:801–816
- 680 Liu ZYC, Zimbelman JR (2015) Recent near-surface wind directions inferred
681 from mapping sand ripples on martian dunes. *Icarus* 261:169–181
- 682 Livingstone I, Warren A (2019) Aeolian geomorphology: an new introduction.
683 Wiley
- 684 Livingstone I, Bristow C, Bryant RG, Bullard J, White K, Wiggs GFS, Baas
685 ACW, Bateman MD, Thomas DSG (2010) The namib sand sea digital
686 database of aeolian dunes and key forcing variables. *Aeolian Res* 2:93–104
- 687 Lorenz R, Claudin P, Andreotti B, Radabaugh J, Tokano T (2010) A 3 km
688 atmospheric boundary layer on titan indicated by dune spacing and huygens
689 data. *Icarus* 205:719–721
- 690 Lü P, Narteau C, Dong Z, Rozier O, Du Pont SC (2017) Unravelling raked
691 linear dunes to explain the coexistence of bedforms in complex dunefields.
692 *Nature comm* 8:1–9
- 693 Lü P, Narteau C, Dong Z, Claudin P, Rodriguez S, An Z, Fernandez-Cascales
694 L, Gadal C, Courrech du Pont S (2021) Direct validation of dune instability
695 theory. *Proc Natl Acad Sci USA* 118
- 696 Mason P, Sykes R (1979) Flow over an isolated hill of moderate slope. *Q J R
697 Meteorol Soc* 105:383–395
- 698 Muñoz-Sabater J, Dutra E, Agustí-Panareda A, Albergel C, Arduini G, Bal-
699 samo G, Boussetta S, Choulga M, Harrigan S, Hersbach H, et al. (2021)
700 Era5-land: A state-of-the-art global reanalysis dataset for land applications.
701 *Earth Syst Sci Data* 13:4349–4383
- 702 Nield JM, King J, Wiggs GFS, Leyland J, Bryant RG, Chiverrell RC, Darby
703 SE, Eckhardt FD, Thomas DSG, Vircavs LH, Washington R (2014) Esti-
704 mating aerodynamic roughness over complex surface terrain. *J Geophys Res*
705 118:12,948–12,961
- 706 Pähzt T, Durán O (2020) Unification of aeolian and fluvial sediment transport
707 rate from granular physics. *Phys Rev Lett* 124:168,001
- 708 Pearce KI, Walker IJ (2005) Frequency and magnitude biases in the 'Fryberger'
709 model, with implications for characterizing geomorphically effective winds.
710 *Geomorphology* 68:39–55
- 711 Pelletier JD, Field JP (2016) Predicting the roughness length of turbulent flows
712 over landscapes with multi-scale microtopography. *Earth Surface Dynamics*
713 4:391–405
- 714 Poggi D, Katul G, Albertson J, Ridolfi L (2007) An experimental investigation
715 of turbulent flows over a hilly surface. *Phys Fluids* 19:036,601
- 716 Rasmussen KR, Iversen JD, Rautaheimo P (1996) Saltation and wind flow
717 interaction in a variable slope wind tunnel. *Geomorphology* 17:19–28
- 718 Raupach M (1992) Drag and drag partition on rough surfaces. *Boundary-layer
719 Meteorol* 60:375–395
- 720 Rubin DM, Hunter RE (1987) Bedform alignment in directionally varying
721 flows. *Science* 237:276–278
- 722 Runyon K, Bridges N, Ayoub F, Newman C, Quade J (2017) An integrated
723 model for dune morphology and sand fluxes on mars. *Earth Planet Sci Lett*

- 724 457:204–212
- 725 Seidel DJ, Zhang Y, Beljaars A, Golaz JC, Jacobson AR, Medeiros B (2012)
726 Climatology of the planetary boundary layer over the continental united
727 states and europe. *J Geophys Research* 117:D17,106
- 728 Shao Y (2008) Physics and modelling of wind erosion, vol 37. Springer Science
729 & Business Media
- 730 Shen Y, Zhang C, Huang X, Wang X, Cen S (2019) The effect of wind speed
731 averaging time on sand transport estimates. *Catena* 175:286–293
- 732 Sheridan PF, Vosper SB (2006) A flow regime diagram for forecasting lee
733 waves, rotors and downslope winds. *Meteorological Applications* 13:179–195
- 734 Sherman D, Farrell E (2008) Aerodynamic roughness lengths over movable
735 beds: Comparison of wind tunnel and field data. *J Geophys Res* 113:1–10
- 736 Sherman DJ, Li B (2012) Predicting aeolian sand transport rates: A reevalu-
737 ation of models. *Aeolian Res* 3:371–378
- 738 Smith AB, Jackson DWT, Cooper JAG (2017) Three-dimensional airflow and
739 sediment transport patterns over barchan dunes. *Geomorphology* 278:28–42
- 740 Song Q, Gao X, Lei J, Li S (2019) Spatial distribution of sand dunes and their
741 relationship with fluvial systems on the southern margin of the taklimakan
742 desert, china. *Geomatics, Natural Hazards and Risk* 10:2408–2428
- 743 Spalding DB (1961) A single formula for the law of the wall. *J Applied Mech*
744 28:455–458
- 745 Stull R (2006) 9 - the atmospheric boundary layer. In: Wallace JM, Hobbs PV
746 (eds) *Atmospheric Science* (Second Edition), second edition edn, Academic
747 Press, San Diego, pp 375–417
- 748 Stull RB (1988) An introduction to boundary layer meteorology, vol 13.
749 Springer Science & Business Media
- 750 Sullivan PP, McWilliams JC (2010) Dynamics of winds and currents coupled
751 to surface waves. *Annu Rev Fluid Mech* 42:19–42
- 752 Sykes RI (1980) An asymptotic theory of incompressible turbulent boundary-
753 layer flow over a small hump. *J Fluid Mech* 101:647–670
- 754 Taylor P, Teunissen H (1987) The Askervein hill project: overview and back-
755 ground data. *Boundary-layer Meteorol* 39:15–39
- 756 Taylor P, Mason P, Bradley E (1987) Boundary-layer flow over low hills.
757 *Boundary-layer Meteorol* 39:107–132
- 758 Ungar JE, Haff PK (1987) Steady state saltation in air. *Sedimentology* 34:289–
759 299
- 760 Unsworth C, Parsons D, Hardy R, Reesink A, Best J, Ashworth P, Keevil G
761 (2018) The impact of nonequilibrium flow on the structure of turbulence
762 over river dunes. *Water Resour Res* 54:6566–6584
- 763 Uppala SM, Källberg P, Simmons AJ, Andrae U, Bechtold VDC, Fiorino M,
764 Gibson J, Haseler J, Hernandez A, Kelly G, et al. (2005) The era-40 re-
765 analysis. *Q J R Meteorol Soc* 131:2961–3012
- 766 Valance A, Rasmussen K, Ould El Moctar A, Dupont P (2015) The physics
767 of aeolian sand transport. *C R Physique* 16:1–13
- 768 Virtanen P, Gommers R, Oliphant TE, Haberland M, Reddy T, Cournapeau
769 D, Burovski E, Peterson P, Weckesser W, Bright J, et al. (2020) Scipy 1.0:

- 770 fundamental algorithms for scientific computing in python. *Nature methods*
771 17:261–272
- 772 Vogelezang D, Holtslag A (1996) Evaluation and model impacts of alternative
773 boundary-layer height formulations. *Boundary-layer Meteorol* 81:245–269
- 774 Vosper SB (2004) Inversion effects on mountain lee waves. *Q J R Meteorol Soc*
775 130:1723–1748
- 776 Walker I, Davidson-Arnott R, Bauer B, Hesp P, Delgado-Fernandez I, Oller-
777 head J, Smyth T (2017) Scale-dependent perspectives on the geomorphology
778 and evolution of beach-dune systems. *Earth-Science Rev* 171:220–253
- 779 Walker IJ, Hesp PA, Davidson-Arnott RG, Bauer BO, Namikas SL, Ollerhead
780 J (2009) Responses of three-dimensional flow to variations in the angle of
781 incident wind and profile form of dunes: Greenwich dunes, prince edward
782 island, canada. *Geomorphology* 105:127–138
- 783 Weaver C, Wiggs G (2011) Field measurements of mean and turbulent airflow
784 over a barchan sand dune. *Geomorphology* 128:32–41
- 785 Wiggs G, Livingstone I, Warren A (1996) The role of streamline curvature in
786 sand dune dynamics: evidence from field and wind tunnel measurements.
787 *Geomorphology* 17:29–46
- 788 Wiggs G, Bullard J, Garvey B, Castro I (2002) Interactions between airflow
789 and valley topography with implications for aeolian sediment transport.
790 *Physical Geography* 23:366–380
- 791 Zhang C, Li Q, Zhou N, Zhang J, Kang L, Shen Y, Jia W (2016) Field obser-
792 vations of wind profiles and sand fluxes above the windward slope of a sand
793 dune before and after the establishment of semi-buried straw checkerboard
794 barriers. *Aeolian Res* 20:59–70
- 795 Zilker DP, Hanratty TJ (1979) Influence of the amplitude of a solid wavy wall
796 on a turbulent flow. part 2. separated flows. *J Fluid Mech* 90:257–271
- 797 Zilker DP, Cook GW, Hanratty TJ (1977) Influence of the amplitude of a solid
798 wavy wall on a turbulent flow. part 1. non-separated flows. *J Fluid Mech*
799 82:29–51

800 **Local wind regime induced by giant linear dunes**
 801 — Supplementary Material —

802 **C. Gadal* · P. Delorme · C. Narteau · G.F.S. Wiggs · M. Baddock ·**
 803 **J.M. Nield · P. Claudin**

804

805 * Institut de Mécanique des Fluides de Toulouse, Université de Toulouse Paul
 806 Sabatier, CNRS, Toulouse INP-ENSEEIHT, Toulouse, France.

807 cyril.gadal@imft.fr

808 **1. Shear velocity and calibration of the hydrodynamical roughness**

809 As the regionally predicted and locally measured velocities are available at
 810 different heights, we can not compare them directly. We ~~then therefore~~ convert
 811 all velocities into shear velocities u_* , characteristic of the turbulent velocity
 812 profile (Spalding 1961; Stull 1988):

$$\frac{u(z)}{u_*} = \frac{1}{\kappa} \ln \left(\frac{z}{z_0} \right), \quad (15)$$

813 where z is the vertical coordinate, $\kappa = 0.4$ the von Kármán constant and z_0 the
 814 hydrodynamic roughness. Several ~~field~~-measurements of hydrodynamic rough-
 815 nesses are available ~~Here cite a few old/general papers on roughness~~(Raupach 1992; Bauer et al. 1992; Brown et al. 2008)
 816 In the absence of sediment transport, it ~~seales with is governed by~~ the geomet-
 817 ric features of the bed (~~Pelletier and Field 2016~~ ~~too specific paper? other older papers?~~).
 818 ~~When transport occurs, it rather typically scales with the thickness of the~~
 819 ~~transport layer. For aeolian saltation, this is~~(Flack and Schultz 2010; Pelletier and Field 2016).
 820 ~~When aeolian saltation occurs, it is rather controlled by the altitude of Bag-~~
 821 nold's focal point (Durán et al. 2011; Valance et al. 2015), which depends on
 822 the wind velocity and grain properties (Sherman and Farrell 2008; Zhang et al.
 823 2016; Field and Pelletier 2018). Whether associated with geometric features
 824 or with sediment transport, its typical order of magnitude is the millimetre
 825 scale ~~on sandy surfaces~~.

826 We do not have precise velocity vertical profiles to be able to deduce an
 827 accurate value of z_0 in the various environments of the meteorological stations
 828 (vegetated, arid, sandy). Our approach is to rather select the hydrodynamic
 829 roughness which allows for the best possible matching between the regionally
 830 predicted and locally measured winds, i.e. minimising the relative difference δ
 831 between the wind vectors of both datasets:

$$\delta = \frac{\sqrt{\langle \|\mathbf{u}_{*,\text{era}} - \mathbf{u}_{*,\text{station}}\|^2 \rangle}}{\sqrt{\langle \|\mathbf{u}_{*,\text{era}}\| \rangle \langle \|\mathbf{u}_{*,\text{station}}\| \rangle}}, \quad (16)$$

832 where $\langle . \rangle$ denotes time average. This parameter is computed for values of z_0
 833 in ERA5-Land analysis ranging from 10^{-5} m to 10^{-2} m for the four different
 834 stations. Note that for the ~~Deep North Sand~~ Sea and South ~~Namib~~ Sand Sea
 835 stations, where the giant dunes feedback presumably affect the wind, we take

836 into account the non-deflected winds only in the calculation of δ (with a 15°
 837 tolerance).

838 As shown in [Suppl. Online Resource Fig. S3S4](#), the minimum values of
 839 δ in the space (z_0^{ERA5Land} , z_0^{local}) form a line. We thus set the roughness in
 840 the ERA5-Land analysis to the typical value $z_0 = 10^{-3}$ m, and deduce the
 841 corresponding ones for the local stations. It leads to 2.7, 0.8, 0.1 and 0.5 mm for
 842 the Adamax, [Deep North Sand](#) Sea, Huab and South [Namib Sand Sea](#) stations,
 843 respectively. Importantly, this approach somewhat impacts the calculation of
 844 the shear velocities, but not that of the wind directions. As such, most of
 845 our conclusions are independent of such a choice. However, it may affect the
 846 magnitude of the wind velocity attenuation/amplification in flow confinement
 847 situations.

848 2. Computation of the ABL characteristics

849 The estimation of the non-dimensional numbers associated with the ABL re-
 850 quires the computation of representative meteorological quantities. In arid
 851 areas, the vertical structure of the atmosphere can be approximated by a well
 852 mixed convective boundary layer of height H , topped by the stratified free at-
 853 mosphere (Stull 1988; Shao 2008). In this context, one usually introduces the
 854 virtual potential temperature T_{vp} , which is a constant T_0 inside the boundary
 855 layer, and increases linearly in the FA ([Suppl. Online Resource Fig. S9S11a](#)):

$$T_{\text{vp}}(z) = \begin{cases} T_0 & \text{for } z \leq H, \\ T_0 \left(1 + \frac{\Delta T_{\text{vp}}}{T_0} + \frac{N^2}{g}(z - H)\right) & \text{for } z \geq H, \end{cases} \quad (17)$$

856 where ΔT_{vp} is the temperature discontinuity at the capping layer and $N =$
 857 $\sqrt{g\partial_z T_{\text{vp}}/T_0}$ is the Brunt-Väisälä frequency, characteristic of the stratification.
 858 Note that, under the usual Boussinesq approximation, temperature and air
 859 density variations are simply related by $\delta T_{\text{vp}}/T_0 \simeq -\delta\rho/\rho_0$ (see [Suppl. Mat.](#)
 860 [of ?Online Resource of Andreotti et al. \(2009\)](#)), so that N can equivalently be
 861 defined from the density gradient as next to Eq. 1.

862 The ERA5 dataset provides vertical profiles of the geopotential ϕ , the
 863 actual temperature T and the specific humidity η at given pressure levels P .
 864 The vertical coordinate is then calculated as:

$$z = \frac{\phi R_t}{g R_t - \phi}, \quad (18)$$

865 where $R_t = 6371229$ m is the reference Earth radius and $g = 9.81$ m s⁻² is the
 866 gravitational acceleration. One also computes the virtual potential tempera-
 867 ture as:

$$T_{\text{vp}} = T \left[1 + \left(\frac{M_d}{M_w} - 1\right) \eta\right] \left(\frac{P_0}{P}\right)^{R/C_p}, \quad (19)$$

where $P_0 = 10^5$ Pa is the standard pressure, $R = 8.31$ J/K is the ideal gas constant, $C_p \simeq 29.1$ J/K is the air molar heat capacity, and $M_w = 0.018$ kg/Mol and $M_d = 0.029$ kg/Mol are the molecular masses of water and dry air respectively. The specific humidity is related to the vapour pressure p_w as

$$\eta = \frac{\frac{M_w}{M_d} p_w}{p - \left(1 - \frac{M_w}{M_d}\right) p_w}. \quad (20)$$

The ERA5 dataset also provides an estimate of the ABL depth H , based on the behaviour of the Richardson vertical profile. This dimensionless number is defined as the ratio of buoyancy and flow shear terms, and can be expressed as $\text{Ri} = N^2 / (\partial_z u)^2$. It vanishes in the lower well-mixed layer where T_{vp} is constant, and increases in the stratified FA. Following the method and calibration of Vogelegang and Holtlag (1996); Seidel et al. (2012), the value $\text{Ri}(z) \simeq 0.25$ has been shown to be a good empirical criterion to give $z \simeq H$ within a precision varying from 50% for the shallower ABL (e.g. at night) to 20% for situations of stronger convection.

Examples of vertical profiles of the virtual potential temperature deduced from ERA5 are shown in [Suppl.-Online Resource](#) Fig. [S9S11a](#). For each of them, an average temperature is computed below the ABL depth ($z < H$), and a linear function is fitted above, allowing us to extract the temperature jump ΔT_{vp} . Importantly, some profiles display a vertical structure that cannot be approximated by the simple form (17) used here ([Suppl.-Online Resource](#) Fig. [S9S11b](#)). In practice, we removed from the analysis all of those leading to the unphysical case $\Delta T_{vp} < 0$. We have noticed that these ‘ill-processed’ profiles dominantly occur in winter and are evenly spread across the hours of the day. Importantly, they represent $\simeq 12\%$ of the data only ([Suppl.-Online Resource](#) Fig. [S9S11c,d](#)), and we are thus confident that this data treatment does not affect our conclusions.

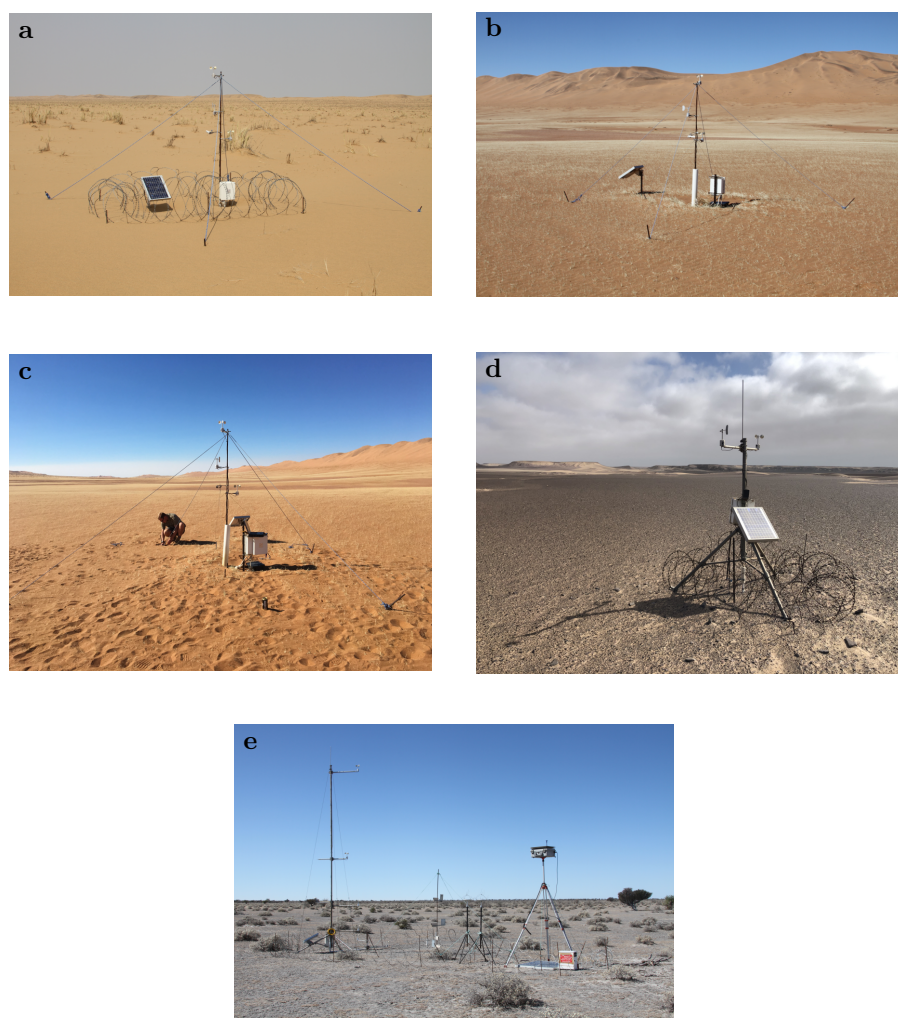


Fig. S1 Photographs of the meteorological stations. **a:** South Sand Sea station. **b–c:** North Sand Sea station. **d:** Huab station. **e:** Adamax station.

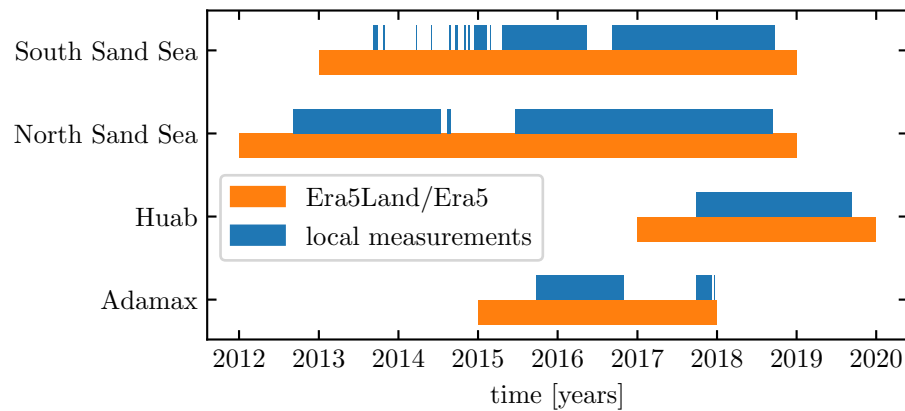


Fig. S2 Gant chart representing the valid time steps for the two data sets, for all stations.

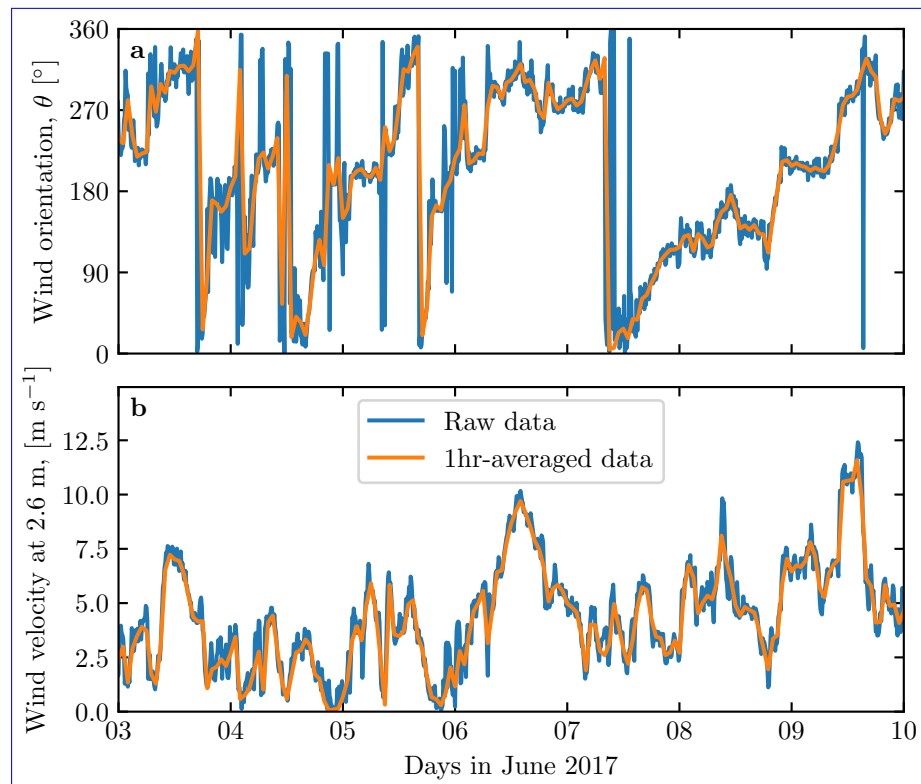


Fig. S3 Comparison between raw local wind measurements, and hourly-averaged data for South Namib-Sand Sea station. **a:** wind direction. **b:** wind velocity at height 2.6 m.

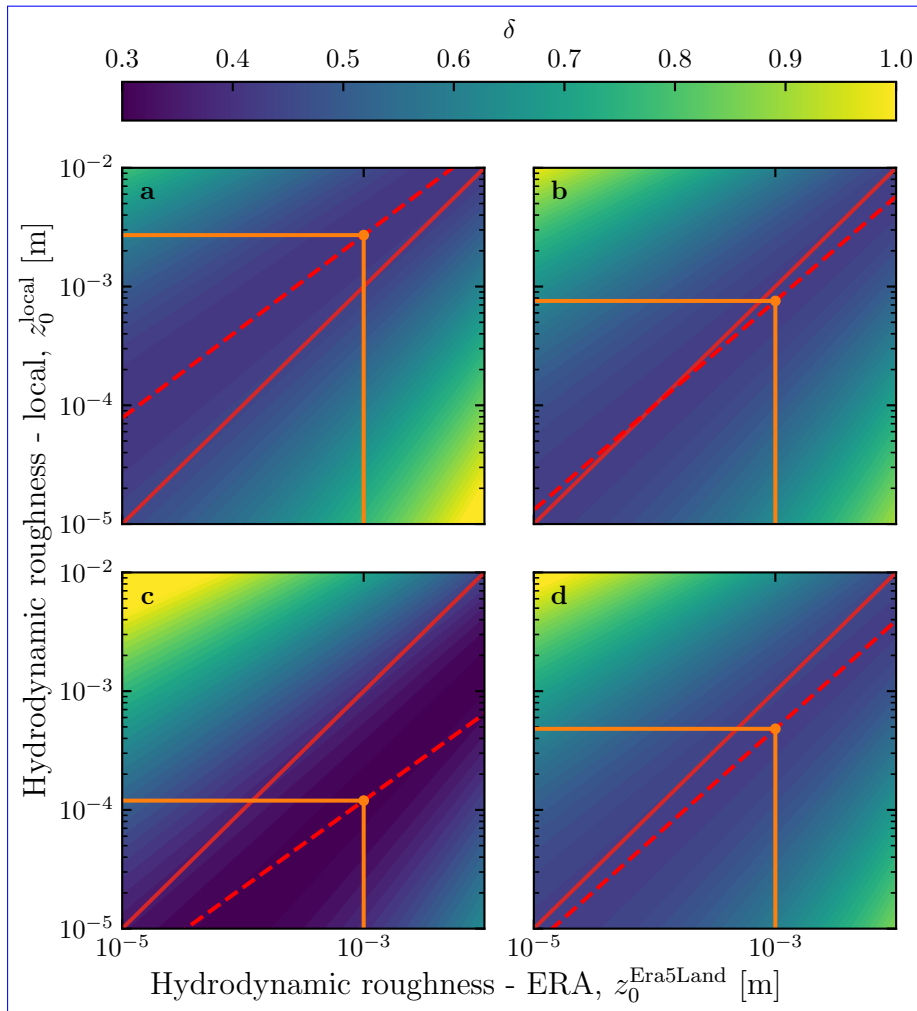


Fig. S4 Calibration of hydrodynamic roughness. The parameter δ (Eq. 16) quantifying the difference between local and predicted winds is shown in colorscale as a function of the hydrodynamic roughnesses chosen for the ERA5-Land and for local winds, for the (a) Adamax, (b) Deep North Sand Sea, (c) Huab and (d) South Namib Sand Sea stations. The red dashed and plain lines shows the minima of δ and the identity line, respectively. The orange lines and dots highlight the chosen hydrodynamic roughnesses for the local winds deduced from setting $z_0^{\text{ERA5Land}} = 1 \text{ mm}$.

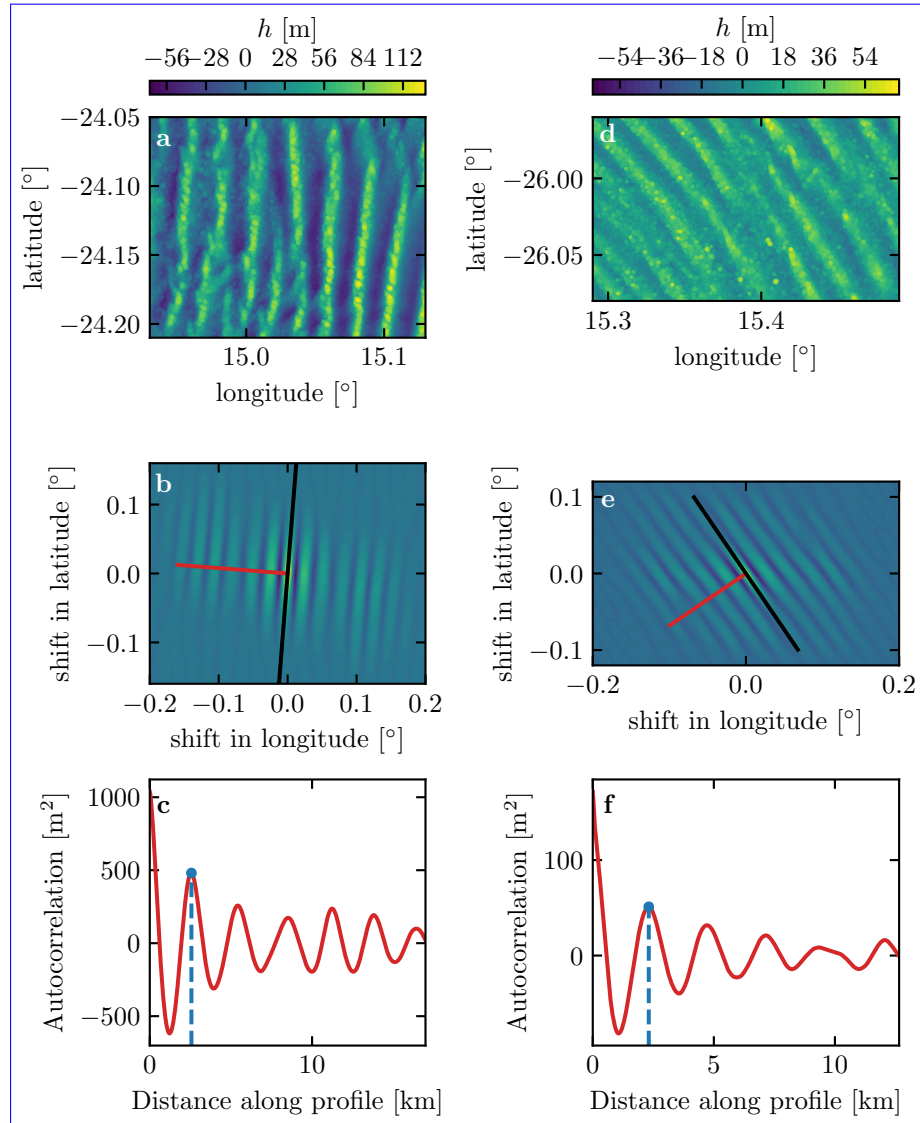


Fig. S5 Analysis of the DEMs of the [Deep North Sand Sea](#) (left column – panels a, b, c) and South [Namib Sand Sea](#) (right column – panels d, e, f) stations. **a-d**: Bed elevation detrended by a fitted second order polynomial base-line. **b-e**: Autocorrelation matrix shown in colorscale. The black line shows the detected dune orientation, and the red line represents the autocorrelation profile along which the dune wavelength is calculated, displayed in **c-f**. The blue lines and dots show the first peak of the autocorrelation profile, whose abscissa gives the characteristic wavelength of the dune pattern.

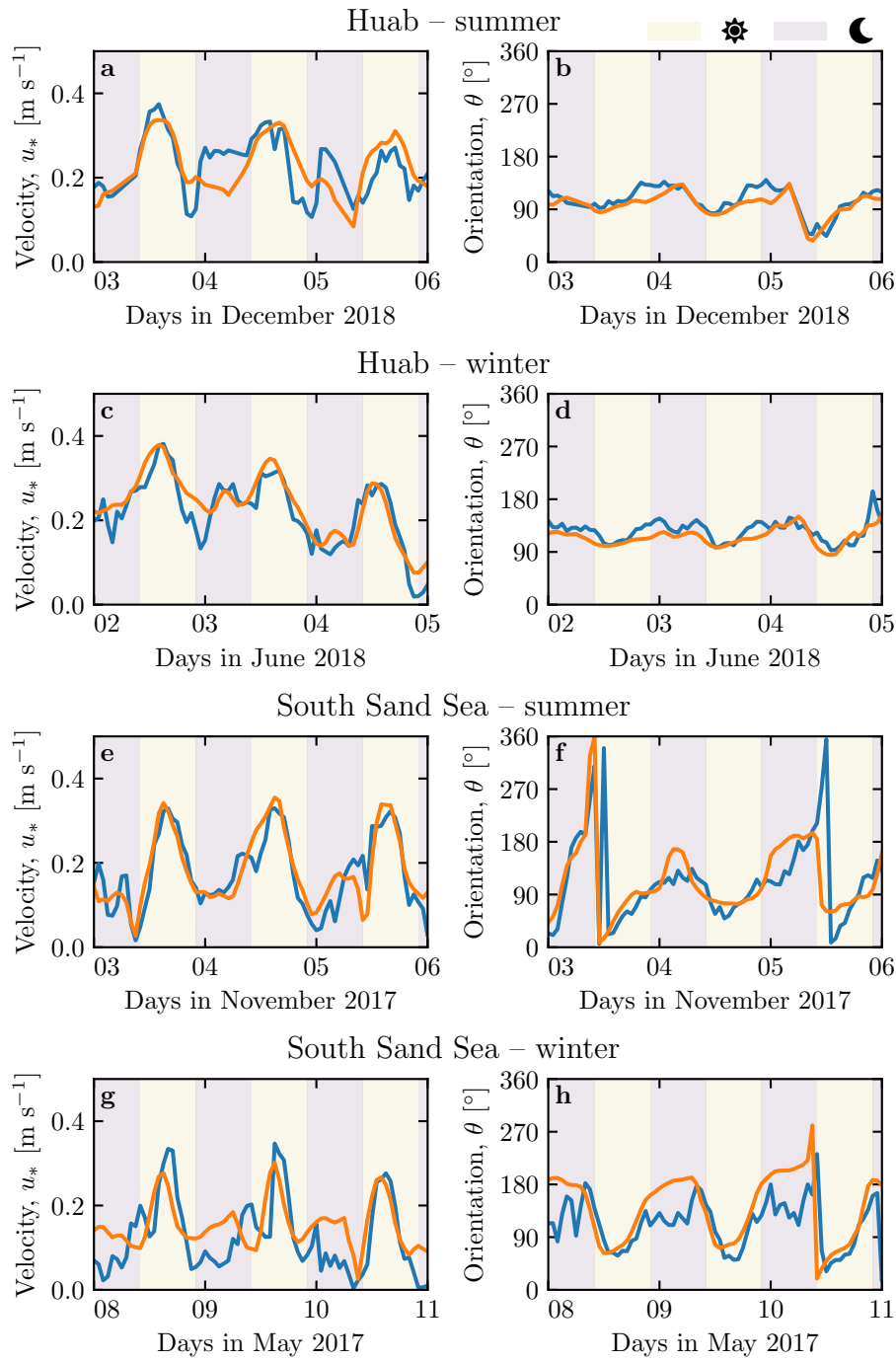


Fig. S6 Temporal comparison between the wind data coming from the ERA5-Land climate reanalysis (orange lines) and from the local measurements (blue lines). Coloured swathes indicate day (between 1000 UTC and 2200 UTC) and night (before 1000 UTC or after 2200 UTC). **a–b:** Huab station in summer. **b–c:** Huab station in winter. **d–e:** South Sand Sea station in summer. **f–g:** South Sand Sea station in winter.

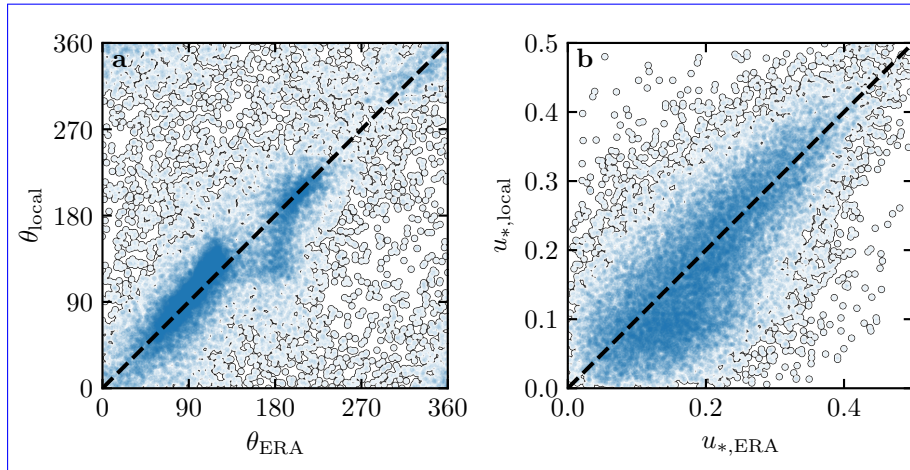


Fig. S7 Statistical comparison of the wind orientation (a) and velocity (b) between the ERA5-Land dataset and the local measurements for the Huab and Adamax stations. Data point clustering around identity lines (dashed and black) provide evidence for agreement of the two sets.

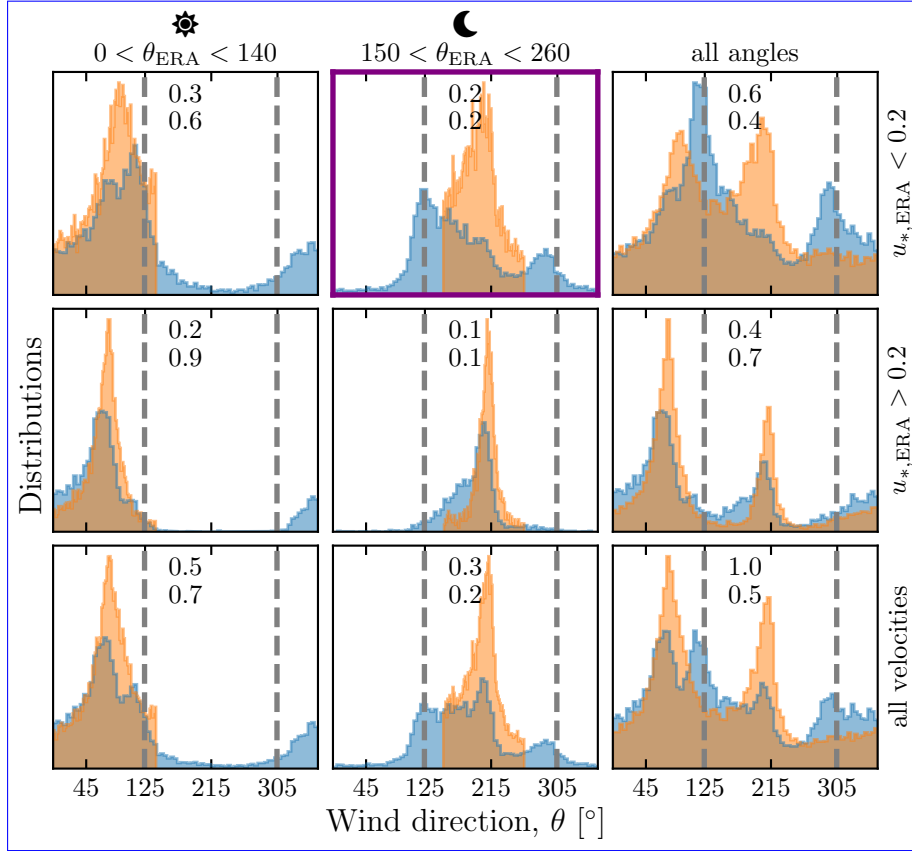


Fig. S8 Distributions of wind direction at the South Namib-Sand Sea Station for the ERA5-Land climate reanalysis (orange) and the local measurements (blue) – equivalent of Fig. 3. In each subplot, both distributions are plotted from the same time steps, selected with constraints on the wind direction (columns) and/or wind velocity (rows) in the ERA5-Land dataset. The gray vertical dashed lines indicate the dune orientation. The numbers at the top centre give the percentage of time steps selected in each sub-range, as well as the percentage of them corresponding to the day (between 1000 UTC and 2200 UTC). The purple frame highlights the regime (small wind velocities, nocturnal summer wind) during which the wind data from both datasets differ.

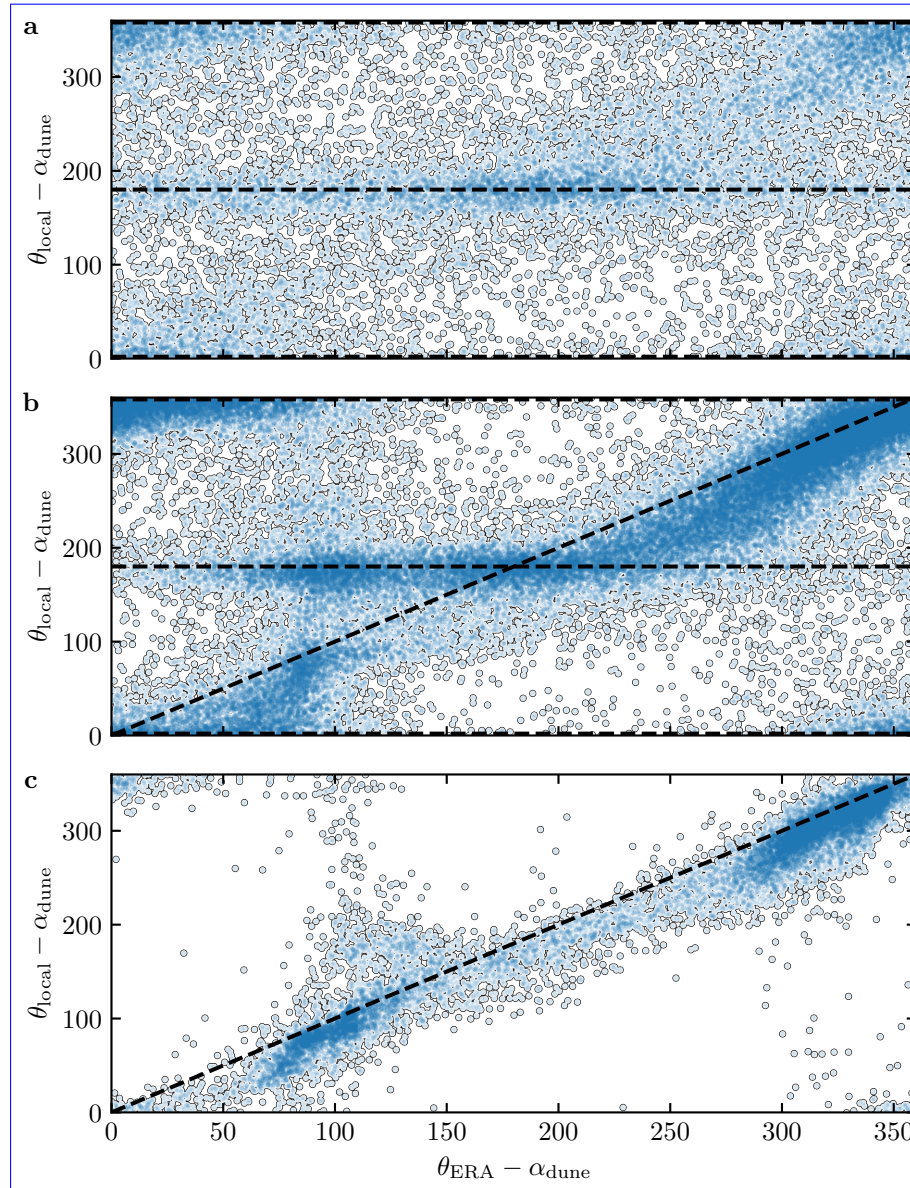


Fig. S9 Statistical comparison of the wind orientation between the ERA5-Land dataset and the local measurements for the South [Namib Sand Sea](#) and [Deep North Sand](#) Sea stations, for different velocity ranges. **a:** $u_{*,\text{ERA}} < 0.1 \text{ m s}^{-1}$. **b:** $0.1 < u_{*,\text{ERA}} \leq 0.25 \text{ m s}^{-1}$. **c:** $u_{*,\text{ERA}} \geq 0.25 \text{ m s}^{-1}$. The measured dune orientations are subtracted to the wind orientation, which allows us to plot both stations on the same graph. Black dashed lines indicate locally measured orientations aligned with the dune crests (here 0° , 180° and 360° – panels **a, b**), as well as the identity lines (panels **b, c**).

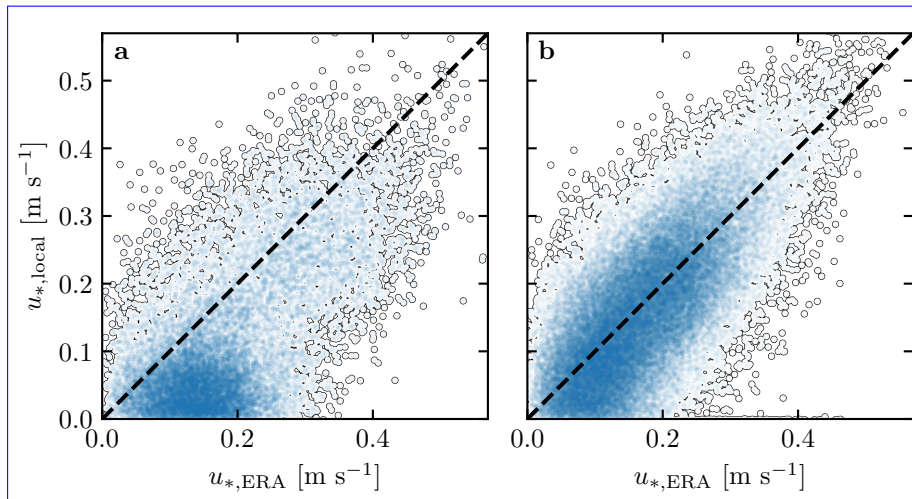


Fig. S10 Statistical comparison of the wind velocity between the ERA5-Land dataset and the local measurements for the South [Namib Sand Sea](#) and [Deep North Sand](#) Sea stations. **a:** Nocturnal summer easterly wind. **b:** Diurnal southerly wind. Black dashed lines are identity lines. The angle ranges used to select diurnal and nocturnal summer winds are the same as those in Fig. 3 and [Suppl.-Online Resource](#) Fig. S6S8.

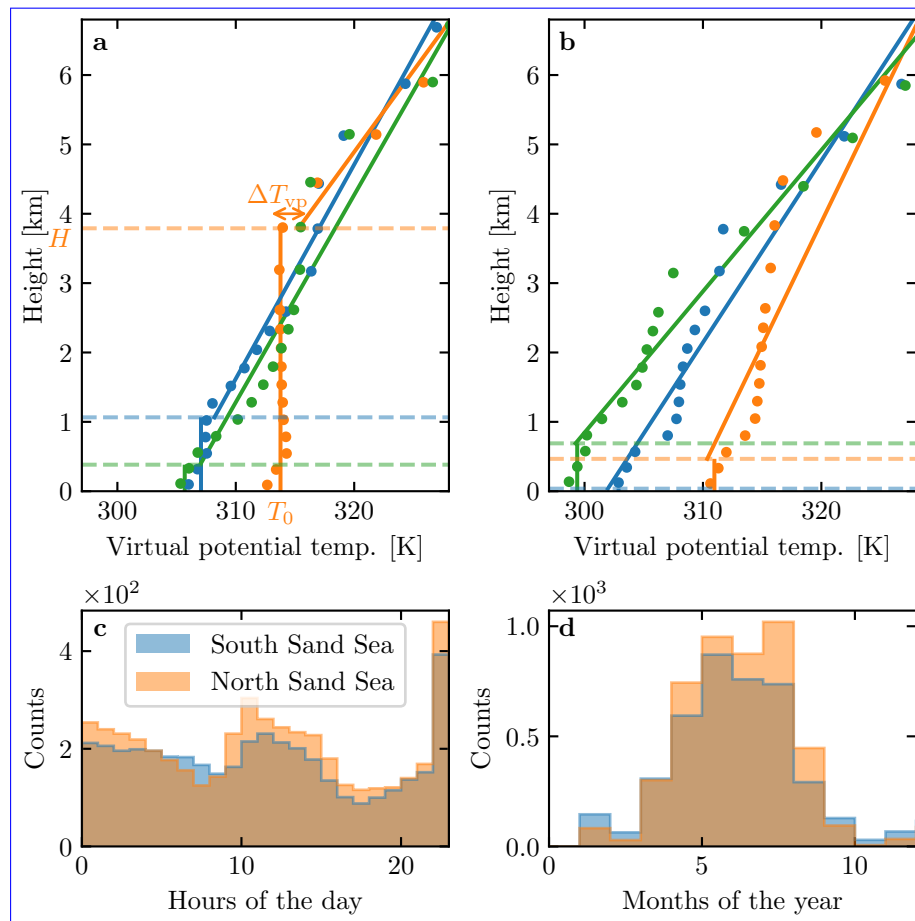


Fig. S11 **a:** Vertical profiles of the virtual potential temperature at three different times (blue: 29/11/2012 - 1100 UTC, orange: 21/03/2017 - 1200 UTC, green: 21/03/2017 - 2000 UTC) at the South [Namib Sand Sea](#) station. Dots: data from the ERA5 reanalysis. Dashed lines: boundary layer height given by the ERA5 reanalysis. Plain lines: vertical (ABL) and linear (FA) fits to estimate the quantities displayed in [Suppl. Online Resource Fig. S10S12](#). **b:** Examples of ill-processed vertical profiles at three different times (blue: 2/12/2013 - 2300 UTC, orange: 20/03/2017 - 0000 UTC, green: 14/07/2017 - 1400 UTC) at the South [Namib Sand Sea](#) station. **c:** Hourly distribution of ill-processed vertical profiles. **d:** Monthly distribution of ill-processed vertical profiles.

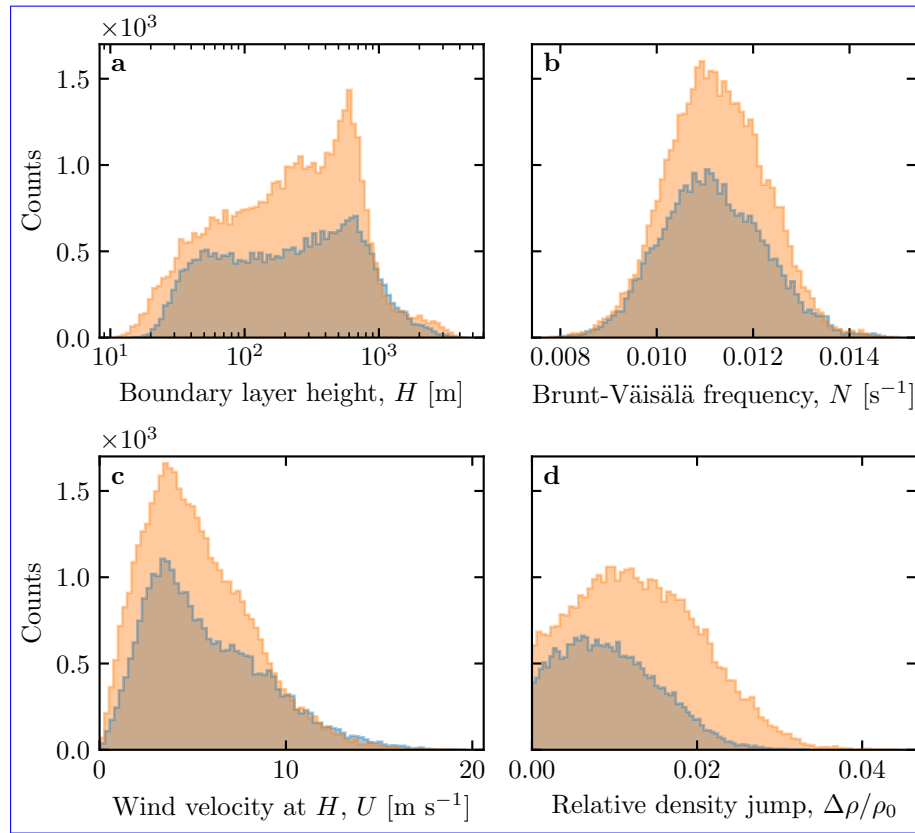


Fig. S12 Distributions of the meteorological parameters resulting from the processing of the ERA5-Land data for the South ~~Namib Sand Sea~~ (blue) and the ~~Deep~~ ~~North~~ Sand Sea (orange) stations. ~~axis label : panel c - velocity at (height) H. Is this for all day/night/seasons ?~~

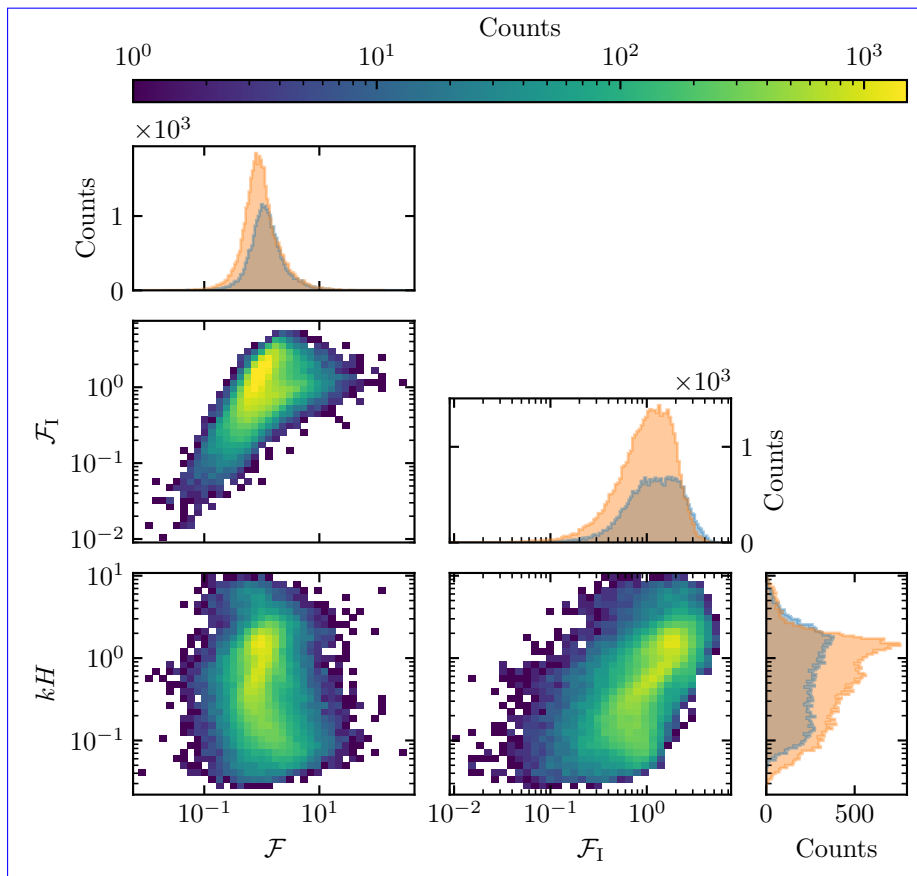


Fig. S13 Non-dimensional parameters distributions. For the marginal [???](#)-distributions, the orange correspond to the South [Namib Sand Sea](#) station, and the blue to the [Deep North Sand](#) Sea station.

Regime diagrams of the wind deviation δ_θ and relative attenuation/amplification δ_u in the spaces (\mathcal{F}_I, kH) and $(\mathcal{F}_I, \mathcal{F})$, containing the data from both the Deep Sea and South Namib stations. Blue dashed lines empirically delimit the different regimes. The point density in each bin of the diagrams is shown in Suppl. Fig. S11. The similar regime diagrams in the space (\mathcal{F}, kH) are shown in Fig. 5.

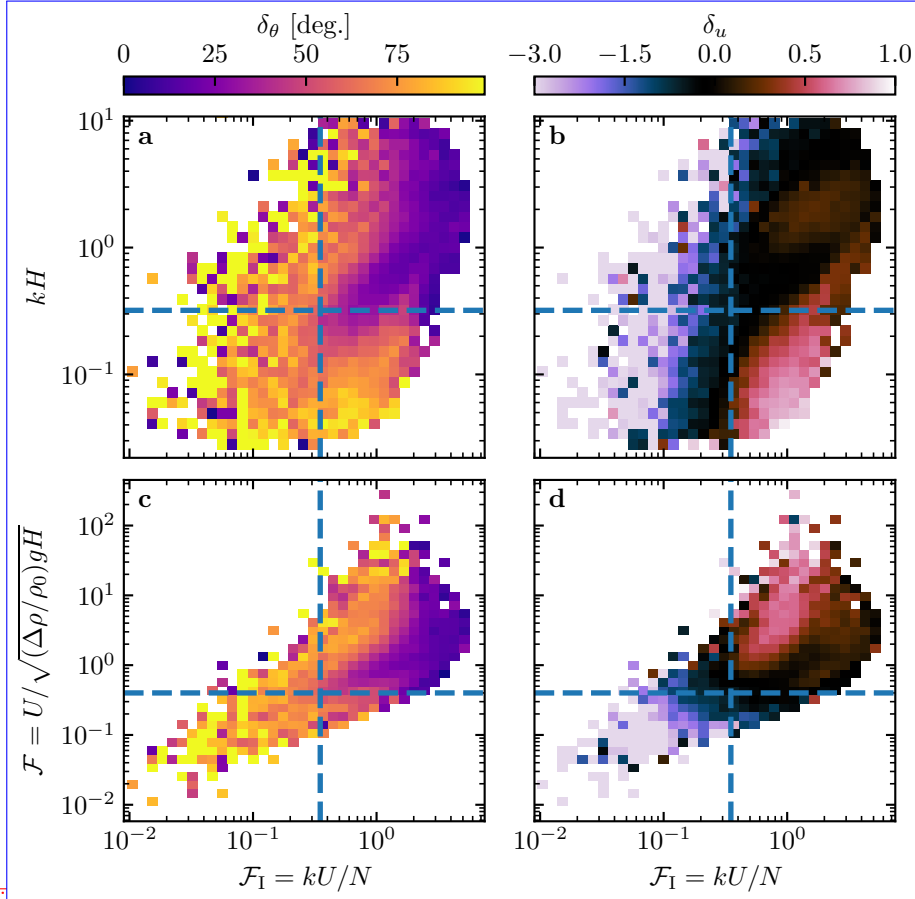


Fig. 5.

Fig. S14 Regime diagrams of the wind deviation δ_θ and relative attenuation/amplification δ_u in the spaces (\mathcal{F}_I, kH) and $(\mathcal{F}_I, \mathcal{F})$, containing the data from both the North Sand Sea and South Sand Sea stations. Blue dashed lines empirically delimit the different regimes. The point density in each bin of the diagrams is shown in Online Resource Fig. S13 – 95% of the data occur in the range $-1 < \delta u < 1$. The similar regime diagrams in the space (\mathcal{F}, kH) are shown in Fig. 5.

~~Computation of the flow disturbance with the linear model of ?.~~ (a) and (b) Magnitude of the hydrodynamic coefficients A_0 and B_0 , calculated from the values of the non-dimensional numbers corresponding to the ERA5 Land time series presented in Figs. 4 and 5. (c) Shear velocity streamlines over sinusoidal ridges of amplitude $k\xi_0 = 0.1$ and for increasing values of $\sqrt{A_0^2 + B_0^2}$. From the upper to the lower streamline, values of $(kH, \mathcal{F}, \mathcal{F}_1, A_0, B_0, \sqrt{A_0^2 + B_0^2})$ are $(1.9, 0.6, 1.5, 3.4, 1.0, 3.5), (1.5, 0.3, 0.4, 4.8, 1.4, 5.0), (0.1, 3.5, 1.0, 8.6, 0.1, 8.6), (0.5, 0.05, 0.04, 9.6, 2.5,$

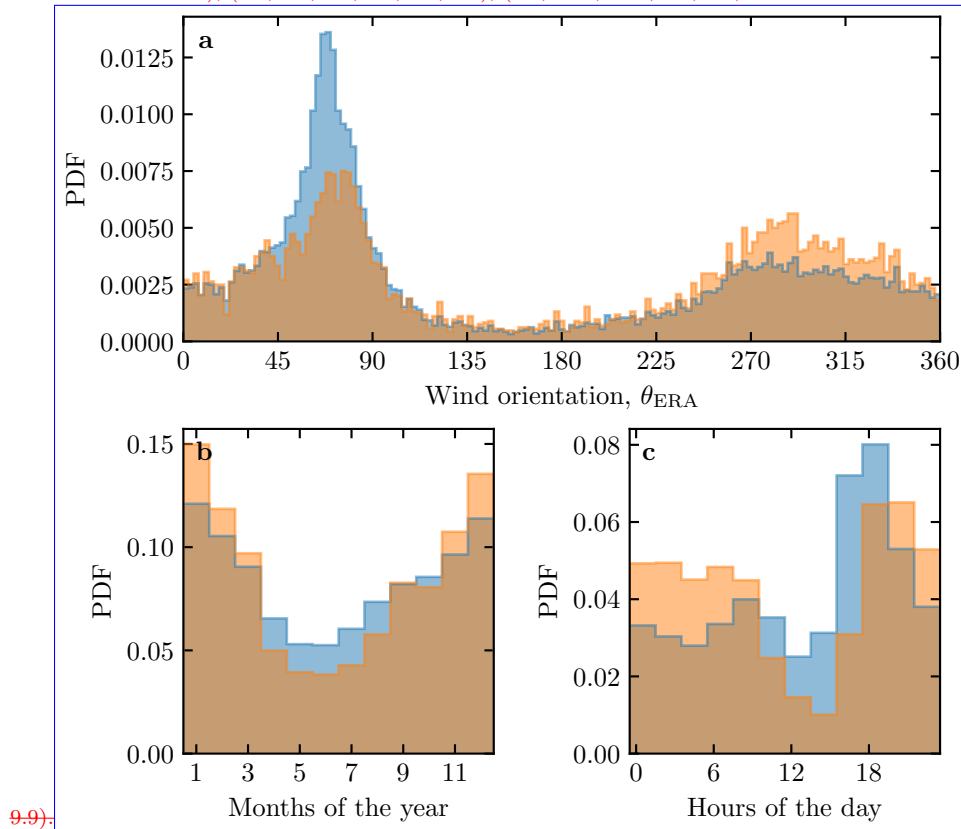


Fig. S15 Normalized distributions of amplified velocities for the North sand Sea (blue: $\delta_u < 0$, orange: $\delta_u < -0.5$). **a:** Angular distributions. **b:** Monthly distributions. **c:** Hourly distributions.

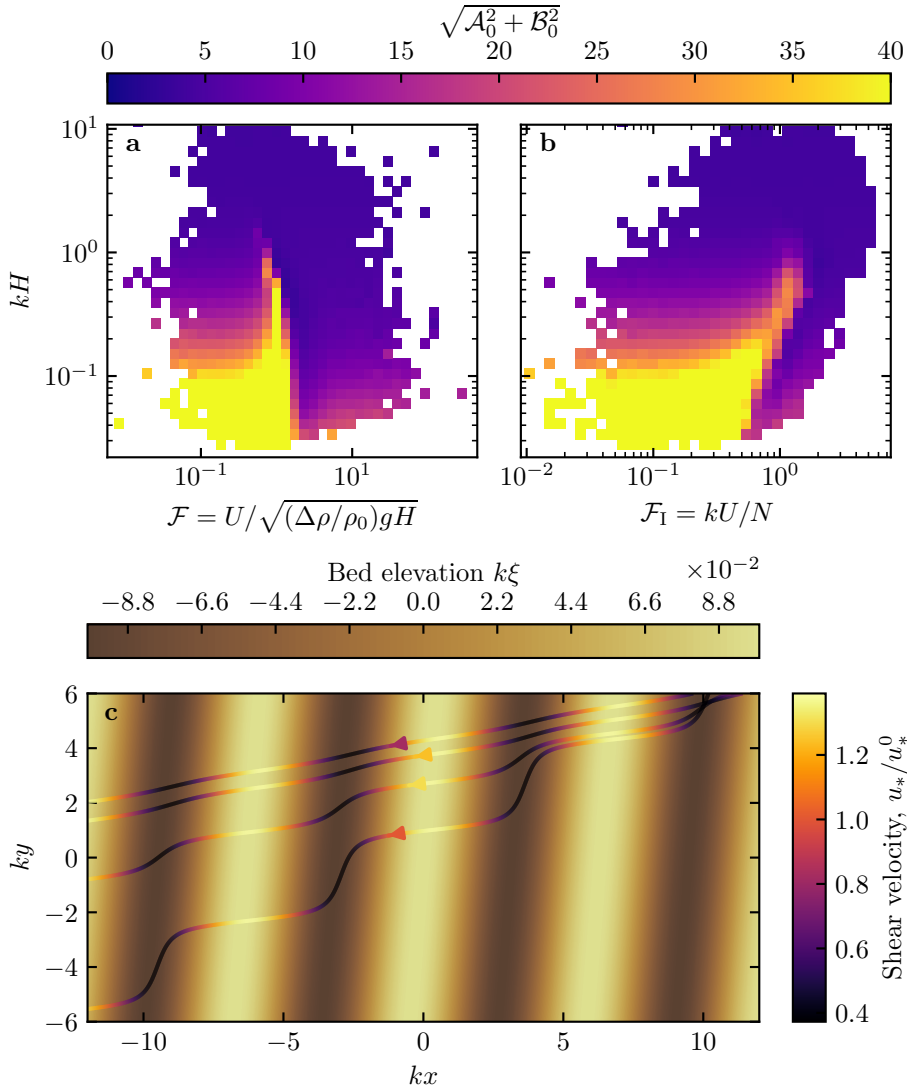


Fig. S16 Computation of the flow disturbance with the linear model of Andreotti et al. (2009). **a** and **b** Magnitude of the hydrodynamic coefficients A_0 and B_0 , calculated from the values of the non-dimensional numbers corresponding to the ERA5-Land time series presented in Figs. 4 and 5. **c** Shear velocity streamlines over sinusoidal ridges of amplitude $k\xi_0 = 0.1$ and for increasing values of $\sqrt{A_0^2 + B_0^2}$. From the upper to the lower streamline, values of $(kH, F, F_1, A_0, B_0, \sqrt{A_0^2 + B_0^2})$ are $(1.9, 0.6, 1.5, 3.4, 1.0, 3.5), (1.5, 0.3, 0.4, 4.8, 1.4, 5.0), (0.1, 3.5, 1.0, 8.6, 0.1, 8.6), (0.5, 0.05, 0.04, 9.6, 2.5, 9.9)$.